Chapter 1
In-situ Characterization of Molecular Processes in Liquids by Ultrafast X-ray Absorption Spectroscopy

Majed Chergui

Abstract The need to visualize molecular and electronic structure in the course of a chemical reaction, a phase transformation a biological function has been the dream of scientists for decades. The development of time-resolved X-ray and electron based methods is making this true. X-ray absorption spectroscopy is ideal for the study of structural dynamics in liquids, because it can be implemented in amorphous media and it is chemically selective. Using X-ray absorption near edge structure (XANES) and extended X-ray absorption fine structure (EXAFS) in laser pump/X-ray probe experiments allows the retrieval of the local geometric structure of the system under study, but also the underlying photoinduced electronic structure changes that drive the structural dynamics. We review the recent development in picosecond and femtosecond X-ray absorption spectroscopy applied to molecular systems in solution: examples on ultrafast photoinduced processes such as intramolecular electron transfer, high-to-low spin change, bond formation and water dynamics are presented.

1.1 Introduction

The advent of femtosecond laser spectroscopy made it possible to observe atomic motions on a time scale that is shorter than a single vibrational period in molecular systems, [1, 2] giving birth to the field of Femtochemistry, which led to the Nobel Prize for Chemistry to Ahmed. H. Zewail in 1999. With femtochemistry, it became possible to follow in real-time molecular and biochemical reactions, phase transitions or coherent oscillations in solids, opening immense insight in our understanding of light-induced phenomena in matter. The impact was huge in

M. Chergui (✉)
Laboratoire de Spectroscopie Ultrarapide ISIC, Faculté des Sciences de Base,
Ecole Polytechnique Fédérale de Lausanne, Station 6, Lausanne, Switzerland
e-mail: majed.chergui@epfl.ch

A. Ziegler et al. (eds.), *In-situ Materials Characterization*,
Springer Series in Materials Science 193, DOI: 10.1007/978-3-642-45152-2_1,

condensed matter physics, in chemistry and in biology, as witnessed to this day by the impressive activity in ultrafast spectroscopy. In femtosecond spectroscopy, a first (pump) laser pulse excites the system at time zero, while a second (probe) pulse probes its evolution as a function of time delay with respect to the pump pulse. However, optical domain spectroscopy does not deliver structure. Thus already in the early days of Femtochemistry, efforts were deployed aimed at implementing the traditional structural tools of X-ray and electron diffraction and of X-ray absorption spectroscopy in time-domain experiments, towards the time resolution of picoseconds to femtoseconds.

The great advantage of electrons is that they scatter on matter 5–6 orders of magnitude more efficiently than X-rays [3]. The techniques of ultrafast electron diffraction, crystallography and microscopy have been pioneered by Ahmed H. Zewail and co-workers, [4–11] who showed the potential and capabilities of these techniques for studying the dynamics of gas phase molecules, surfaces, interfaces, biological systems and in materials science. In particular, the tools of ultrafast electron microscopy have heralded a real revolution by allowing real-time and real-space imaging of photoinduced effects. In addition, novel methods keep being added to the tool-kit of electron-based techniques, such as ultrafast EELS, [12, 13] which now allows the visualization of the electronic structure changes together with the geometric changes and therefore relate the two or the Photoinduced near-field electron microscopy (PINEM) approach, [14] which allows visualization of the electric field around photoexcited species. New developments are also possible using relativistic ultrafast electrons to probe matter [15]. In summary, electron-based ultrafast research is a new area of research with ramifications into very diverse fields thanks to a broad range of methods [16]. Last but not least, electron techniques are all lab-based, which offers a great flexibility and versatility.

The high scattering cross-section of electrons versus X-rays, also implies that they are not very penetrating (except for relativistic ones) compared to the latter, so that they are not ideal to probe bulk dynamics, for which ultrashort X-ray pulses seem more appropriate. There are two main classes of sources of ultrashort X-ray pulses: lab-based ones and large-scale installations, such as synchrotrons and very recently, X-ray free electron lasers (X-FEL). The lab-based sources mainly consist of plasmas, which are generated when an intense femtosecond laser pulse hits a metal target, delivering X-ray pulses of 100's fs. However, the ensuing X-ray emission is isotropic, polychromatic, low flux, and the source is unstable on a pulse-to-pulse basis. Synchrotron sources provide fairly high fluxes of very stable, tunable and collimated X-rays, but the pulse width is in the 50–100 ps range. They have been used at this time resolution for molecular and protein crystals [17–23] as well as for scattering studies of molecules in solution [24–30]. Recently, with the advent of the slicing scheme, [31–34] femtosecond pulses of monochromatic X-ray photons are also available at synchrotrons, that have been used for both X-ray diffraction studies [35] and X-ray absorption spectroscopy ones [36–39].

Ultrafast X-ray diffraction has been used to study coherent lattice dynamics, strain propagation, melting phenomena and phase transitions in bulk materials and in nanostructures [35, 40–47]. As mentioned above, protein and molecular crystals

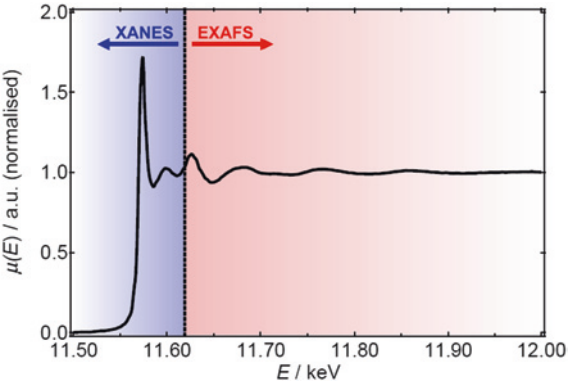

Fig. 1.1 X-ray absorption spectrum at the L_3 edge of a diplatinum complex (Pt_2POP) in solution [206] illustrating the low-energy XANES *region* up to ~50 eV above the ionization potential (IP) and the high-energy EXAFS *region* >50 eV above the IP. The first peak at the edge is due to a bound–bound 2p-5d transition, [207] and the IP lies above it

have been investigated with 100 ps to ns time resolution, while the first studies at higher temporal resolution are starting to appear on such systems [48–50]. X-ray diffraction of liquids initially proposed by Wilson and co-workers [51–53] has so far been limited to the 100 ps resolution [29, 54] and is challenging due to heating, lack of long-range order, the presence of several photoproducts and the high background of light scattered by the solvent and the unexcited species. The studies carried out at synchrotrons are however crucial as they prepare the ground for the implementation of similar experiments with femtosecond resolution at the new and intense sources of X-rays, such as the X-ray free electron lasers (XFELs).

Chemistry and biology mainly occur in the condensed phases and in particular, liquids. It is thus important to probe the chemical and biochemical dynamics in this environment. Furthermore, molecular (geometric) structure changes are triggered and/or accompanied by electronic structure changes, either under excitation by light or in the presence of a reactant. Ideally, one would like not only to probe the *molecular structure* changes in real-time, but also identify the *electronic structure* changes underlying them. In recent years, time-resolved X-ray absorption spectroscopy (XAS) has emerged as an ideal tool for the study of structural dynamics in liquids [10, 30, 36, 55–61]. The present contribution is about these developments and new ones to come. We purposely limited ourselves to studies carried out at fs to sub-ns resolution.

1.2 X-ray Absorption Spectroscopy

X-ray absorption spectra are characterized by absorption edges, which are element specific and reflect the excitation of core electrons to the ionization threshold [62–64]. At a given edge, the spectrum consists of bound–bound transitions below the ionization potential (IP) of the inner-shell electron, followed by the absorption edge jump itself (Fig. 1.1). Right above the absorption edge one observes a complicated modulation of the absorption cross section due to multiple scattering of the ionized photoelectron

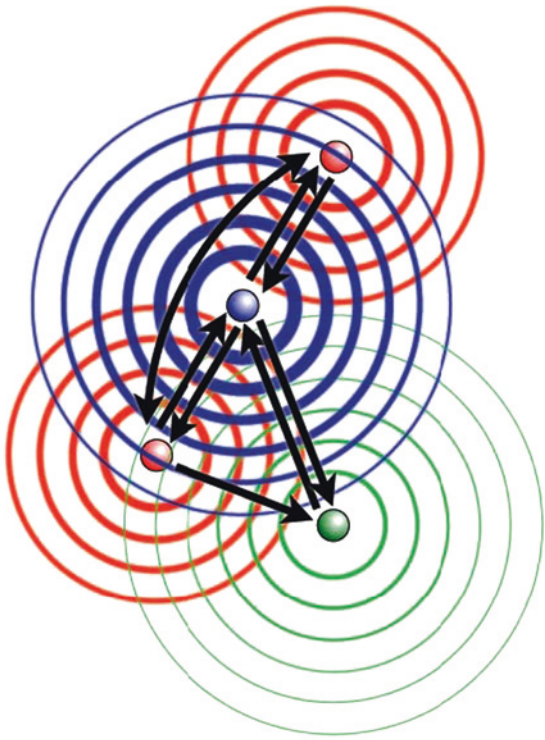

Fig. 1.2 Pictorial view of the single- and multiple-scattering pathways of an outgoing photoelectron wave (*blue*) off 1st-shell (*red*) and 2nd-shell (*green*) neighboring atoms. The strength of the scattered wave is reflected in the line thickness

by its nearest neighbors in the molecule. The spectral range around the edge is called the XANES region (X-ray absorption near-edge structure), and it contains rich information about both the electronic (below the IP) and the geometric structure (above the IP) including bond angles and distances (Fig. 1.1).

From about 50 eV above IP to higher energies mainly single scattering events dominate, which result in a weak oscillatory modulation of the absorption cross section. This region is called the EXAFS region (Extended X-ray Absorption Fine Structure). It delivers precise information about the internuclear distance of the nearest neighbors from the absorbing central atom. Oscillations therefore do not exist in the case of the isolated atom. Thus a single spectrum contains simultaneously information about the valence electronic structure and about the nuclear arrangement of the atoms in the molecular system (Fig. 1.2).

1.2.1 Extended X-ray Absorption Fine Structure (EXAFS)

In the energy regime of EXAFS, the photoelectron states approximate to spherical waves. EXAFS is a final-state quantum-interference effect involving scattering of the outgoing photoelectron from the neighbouring atoms, and the oscillatory

structure is due to the interference between the outgoing photoelectron wave and the wave scattered back at neighboring atoms (Fig. 1.2). At high photoelectron kinetic energies, the scattering of electrons is such that the only significant contributions to the final state wave function in the vicinity of the absorbing atom comes from paths, in which the electron is scattered only once (single scattering events) [65]. The photoelectrons emitted from the excited atom as spherical waves damp out rapidly due to inelastic effects caused by the extended valence orbitals of the nearby-lying atoms. This limits the probed spatial region and, it ensures that multiple-scattering effects beyond simple back-scattering can be ignored. This allows the analysis of the data by a simple Fourier transformation [66]. For this purpose one has to generate an X-ray absorption spectrum, normalized to the absorption edge jump under consideration, which is defined as the normalized oscillatory part of μ(E) (the X-ray absorption coefficient), i.e. the EXAFS, via

$$\chi(E) = \frac{[\mu(E) - \mu_0(E)]}{\Delta\mu_0(E)} \tag{1.1}$$

with $\mu_0(E)$ being the smoothly varying atomic-like background absorption and $\Delta\mu_0$ is a normalization factor that arises from the net increase in the total atomic background (or simply the absorption edge jump). Substituting E above the edge with the photoelectron wave vector, we can rewrite $\chi(k)$ as

$$\chi(k) = \sum_j S_0^2 N_j \frac{|f_j(k)|}{kR_j^2} \sin\left[2kR_j + 2\delta_e + \Phi\right] \cdot e^{-\frac{2R_j}{\lambda(k)}} \cdot e^{-2\sigma_j^2 k^2} \tag{1.2}$$

which is the standard EXAFS formula. The structural parameters (for which the subscript j refers to the group of N_j atoms with identical properties, e.g., bond distance and chemical species) are:

(a) the interatomic distances R_j,
(b) the coordination number (or number of equivalent scatterers) N_j,
(c) the temperature-dependent *rms* fluctuation in bond length σ_j, which should also include effects due to structural disorder.
(d) $f_j(k) = |f_j(k)|e^{i\phi(k)}$ is the backscattering amplitude, δ_e is central-atom partial wave phase shift of the final state, and $\lambda(k)$ is the energy-dependent photoelectron mean free path (not to be confused with its de Broglie wavelength), and S_0^2 is the overall amplitude factor.

Moreover, although the original EXAFS formula referred only to single-scattering contributions from neighboring shells of atoms, the same formula can be generalized to represent the contribution from N_R equivalent multiple-scattering contributions of path length $2R$ [64].

Equation 1.2 contains all of the key elements that provide a convenient parametrization for fitting the local atomic structure around the absorbing atom to the measured EXAFS data. The dependence of the oscillatory structure on interatomic distance and energy is clearly reflected by the sin($2kR$) term. The decay of the wave due to the mean free path or finite lifetime (including the ultrashort

core–hole lifetime) of the photoelectron is captured by the exponential term $e^{-2R/\lambda}$. The strength of the reflected interfering waves depends on the type and number of neighboring atoms and is given by the backscattering amplitude $|f_j(k)|$ and hence is primarily responsible for the intensity of the EXAFS signal. Other factors, namely, the spherical-wave factors $(1/kR^2)$ and mean-free-path terms, appear secondary but are important for a quantitative description of the EXAFS amplitude. The phase factor $\Phi = \arg f(k)$ reflects the quantum–mechanical wavelike nature of the backscattering process. The $\exp(-2\sigma^2k^2)$, representing the Debye–Waller broadening to a good approximation, is partly due to thermal effects, which cause the atoms to jiggle around their equilibrium atomic positions. These slight movements smear out the otherwise sharp interference pattern of the rapidly varying $\sin(2kR)$ term with increasing k. Effects of structural disorder are similar and they give an additive contribution to σ^2. The Debye–Waller effect seems more pronounced at shorter photoelectron wavelengths and hence it terminates the EXAFS at sufficiently large energy beyond $k \sim 1/\sigma$, which is typically around 10 $Å^{-1}$. Finally, S_0^2 is a many-body effect due to the relaxation of the system in response to the creation of the core hole. It is usually approximated by a constant. Using 1.2, it can be seen that a Fourier transform of the EXAFS with respect to k corresponds to an effective radial distribution function, with peaks near the first few nearest neighbor distances, provided the phase shifts are correctly dealt with. Other improvements to the theory have been amended, such as multiple scattering and curved-wave effects [64].

For disordered system, Filipponi [67] has derived an equivalent of (1.2) that uses an integral over the radial distribution function (g) rather than a discrete sum:

$$\chi(k) = \sum_i \int_0^\infty 4\pi\rho_i r^2 g_{X-S_i}(r) A_i(k,r) \sin(2kr + \varphi_i(k,r)) dr \tag{1.3}$$

where X is the absorber (e.g., solute), i stands for a given atom of the solvent species. $A(k,r)$ and $\phi(k,r)$ are the amplitude and phase functions. An average solvation shell structure, described by radial pair distribution functions between the (in this case, atomic) solute and each class of solvent atom, can be extracted from the analysis of the EXAFS signal using this equation. Theoretical EXAFS signals associated with each type of solvent atom of the first shell molecules, are calculated from (1.3) using standard packages. The phase shifts $\phi(k,r)$ are calculated from a snapshots of atomic coordination given by molecular dynamics simulations. The $\chi(k)$ signal is mainly sensitive to a limited distance from the absorber (A) due to the finite photoelectron mean-free path, this effect together with the spectral damping due to monochromator resolution are included in the scattering amplitude $A(k,r)$.

1.2.2 X-ray Absorption Near Edge Spectroscopy (XANES)

In contrast to the EXAFS region, for which accurate quantitative results are generally routine, both the calculation and interpretation of XANES have remained

challenging tasks. The complications arise from the low kinetic energy of the photoelectron in this region resulting in large scattering amplitudes (and consequently multiple scattering events, Fig. 1.2) and the necessity to adequately describe many-body effects. In addition, the photoelectron energy is comparable to the fine details of the atomic Coulomb potential which renders the XANES spectrum very sensitive to inaccuracies of the simplified model that is chosen to represent the atomic potentials. With the development of an efficient self-consistent, relativistic and full multiple scattering code (FEFF) by Rehr and coworkers, [64, 68, 69] the theoretical errors in XANES calculations are largely reduced making a (semi-) quantitative interpretation of the spectral features possible. This is achieved in particular by the efficient many-pole representation of the system dielectric function in order to account for intrinsic and extrinsic inelastic losses of the photoelectron [70] and the possibility to use full potentials instead of the simplified muffin-tin (MT) approximation [71, 72].

In general, XAS, in the single electron and dipole approximations, probes the probability of a dipole-mediated transition of a deep core electron $|i\rangle$ of the absorbing atom into some unoccupied state $|f\rangle$ above the Fermi level E_F. The measured X-ray absorption cross section $\mu(E)$ is described by the Fermi golden rule

$$\mu(E) \propto \sum_{f}^{E_f > F_F} \left| \left\langle f \left| \widehat{\varepsilon} \cdot \vec{r} \right| i \right\rangle \right| \delta\left(E - E_f\right) \tag{1.4}$$

where $\widehat{\varepsilon} \cdot \vec{r}$ is the dipole operator of the incoming light and the sum is over all energies above the Fermi level. There are two general strategies for solving this equation in order to calculate the XAS spectrum [70, 73]. The first implies accurately expressing the deep core state $|i\rangle$ and final states $|f\rangle$ in terms of wave functions and then explicitly evaluating the sum of (1.4). This is essentially the approach adopted by molecular orbital theories, but it is limited by the accurate description of the final state. This limitation is avoided by the second strategy adopted by multiple scattering theories for which (1.4) is rewritten using a single-particle Green's function operator $G = [E - H]^{-1}$, where H is the effective one-electron Hamiltonian and E is the photoelectron energy. The use of the Green's function formalism as a tool to avoid the explicit representation of final states is the basis of Multiple Scattering theory which originated in the 1970s [74, 75]. One of the approximations is to write the total Hamiltonian of the system as $H = H_0 + V_{int} + \delta V$, where V_{int} is a flat interstitial potential due to the system of ions and electrons in a given system. The ions are the scattering sites of potential δV. The scattering atomic potentials H_0 are approximated with spherically symmetric Coulomb-type potentials embedded within the interstitial potential V_{int}. This approximation is called *muffin-tin* (MT) potential approximation. Within the MT approximation, the electron wavefunction can be expressed by spherical harmonics with an additional radially dependent part, which extends into the V_{int} region. The outer region sets the specific boundary conditions onto the electron wave function acting within the cluster sketched. The Multiple Scattering equations derived from this approach are the basic ingredients of the computer codes used in XAS calculations, which consist of mainly two families: the FEFF and

MXAN codes. Both programs allow computing the XAS spectra within the MT approximation used in Multiple scattering theory and in addition they can be used to fit the experimental spectra given the initial structure of the atomic cluster [68, 74, 76].

Several key developments have increased the accuracy of the calculations, offering the possibility to interpret XANES either in terms of local electronic structure or within a XAFS-like scattering picture [70]: (1) the use of full multiple-scattering (FMS) cluster calculations of both XAS and DOS; (2) the use of self-consistent field (SCF) potentials (both of these developments are based on Green's function calculations); (3) ab initio calculations of many-body intrinsic and extrinsic inelastic losses of the photoelectron. More details are found in the cited papers, in particular [69].

A crucial point in all time-resolved X-ray studies is the extraction of the excited state spectrum from the transient (difference transmission with the above described scheme) spectra, which is a prerequisite for the structural analysis. Naturally, this is strongly sensitive to the precise determination of the photoexcitation yield, as this may induce errors in the structural determination [58]. In the simple case of a mere two-level system, the analysis uses the XAS spectrum of the ground and (extracted) excited state. Several codes exist that fit both the XANES [64, 68, 70, 77–81] and the EXAFS [64, 82] regions. However, quite frequently it is difficult, if not impossible, to extract the excited state fractional population from comparative optical-only studies, because the ground state bleach (GSB) is often overlapped by excited state absorption (ESA) or stimulated emission (SE). In addition, populations extracted from laser-only studies need to be convoluted with the much longer X-ray pulse width, giving rise to additional ambiguities.

An alternative approach was developed that fits the transient EXAFS spectrum in energy space directly [83]. A series of EXAFS spectra are simulated for a collection of possible excited state structures from which the ground state fit spectrum is subtracted to generate transient spectra. These are then compared with the experimental TA spectrum using a least-squares statistical analysis to derive the structural change. This approach reduces the number of required parameters by cancellation in the differences. It can also deliver a unique solution for both the fractional population and the extracted excited state structure, next to quantifying electronic information about possible energy shifts [83]. A similar approach was also proposed for fitting difference XANES spectra [80]. It is however clear that one needs to have a preconceived idea of the input structures, which are based on knowledge of the system and its realistic deformation geometries, as for example in the case of bimetallic complexes (see Sect. 1.4.2).

Concerning the electronic structure information from the bound–bound XANES features, the charge transfer ligand field multiplet theory [84–87] has proven very successful on a wide range of systems, both in molecular and condensed matter physics. The theory takes into account all Coulomb interactions as well as the spin–orbit coupling between the atomic orbitals, and treats the geometric environment of the absorbing atom through a ligand field potential. It also introduces orbital mixing between the central atom and its ligands via charge

transfer terms. This tool has now been extended to model excited state XANES spectra [88] but here too, the comparison with experiment is critically dependent on a most accurate determination of the fraction of excited state population [58].

Summarising this section, XANES and EXAFS are useful to extract the following type of information:

a. The bound–bound XANES features are due to transitions from core orbit also to valence ones, and the latter are involved in chemical bonding and/or are transformed under visible-ultraviolet light excitation. Thus one can interrogate the occupancy of valence orbitals, the oxidation state of the system, the occurrence of charge transfer processes, orbital delocalization, bonding and back-bonding contributions, etc. [63, 87, 89], and their changes in the course of a chemical, biochemical or physical transformation.
b. Above ionization XANES multiple scattering resonances (also called shape resonances [63]) can deliver information about bond distances and angles, as well as coordination numbers [71, 90–92].
c. The single scattering EXAFS region delivers information about bond distances and coordination numbers of the nearest neighbours around the absorbing atom. The structural analysis of EXAFS is much simpler than that of XANES, which is the reason why EXAFS is more commonly used in static studies of molecular structure, even though the EXAFS modulations are typically less than 10 % of the edge jump.

Furthermore, XAS (XANES and EXAFS) offers the following advantages:

i. it is atom selective
ii. it can detect species that are spectroscopically silent in the optical domain
iii. it can be implemented in any phase of matter (gas, liquid, solid) and in biological systems
iv. it delivers information about both the electronic and the geometric structure of the system under study
v. the information about geometric changes is local (i.e. one to three shells of neighbours around the species of interest), but this is not a problem since ultrashort time scales correspond to ultrashort distance changes.

In the past 10 years, time-resolved XAS of liquids systems has matured to a routine method on the picosecond time scale, [10, 55–58, 93] while the femtosecond time resolution has just been achieved, [36, 39] opening exciting perspectives for ultrafast structural dynamics of chemical and biological systems in liquids.

1.3 Methodology

For time-resolved X-ray absorption spectroscopy, the X-ray source should ideally fulfill the following requirements: (1) continuum radiation covering the range from soft to hard X-ray energies; (2) ultrashort pulses; (3) high photon fluxes; (4)

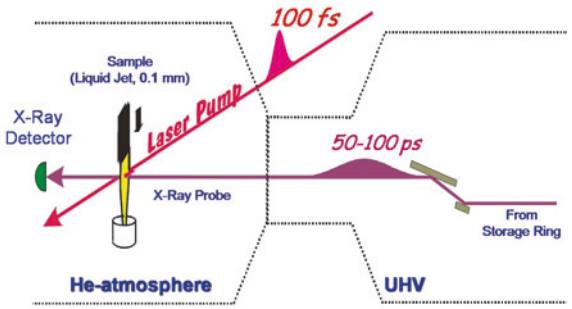

Fig. 1.3 experimental lay out of an optical pump/X-ray absorption probe experiment at a synchrotron

high pulse-to-pulse, as well as long term stability; (5) synchronization to an external light source (e.g., a pump laser). The only X-ray sources that approach these requirements are 3rd generation synchrotron storage rings, albeit at the cost of a lower temporal resolution (tens of ps). However, the sub-ps range has been achieved at synchrotrons thanks to the implementation of the so-called slicing scheme [31, 33, 34, 94] though at a largely reduced photon flux.

There has been several attempts to use plasma sources of X-rays for ultrafast XAS experiments ever since the beginning of the 1990s, [95–104] but these never materialised into a routine methodology as much as the synchrotron-based approach did. This has to do with the experimental difficulties and limitations inherent to plasma sources that have large pulse to pulse fluctuations, low fluxes at a given energy bandwidth as well as limited spectral tunability. Synchrotron based X-ray absorption experiments have had more success and are now routinely used at the SLS (Villigen), APS (Argonne), ALS (Berkeley) and BESSY (Berlin), while more experiments are being implemented. However, plasma-based sources have had (and still have) much success in ultrafast X-ray diffraction studies [42, 43, 45, 105].

The development and methodology of time resolved XAS studies at synchrotrons have been described in refs [10, 55–59, 106–110]. The now commonly used approach was implemented by the Lausanne group. It is based on recording the transient (difference) absorption on a pulse-to-pulse basis. Briefly (Fig. 1.3), monochromatic X-rays are focussed to 50–100 μm diameter onto the sample. X-ray signals are detected with large-area avalanche photodiodes (APD), of which one for transmission (I_1) and one for the incident signal (I_0) scattered off a thin metal foil, and two (or more, if space allows) fluorescence APDs (I_{F1}, I_{F2}) for the X-ray fluorescence from the sample. The sample consists of a free-flowing liquid jet, which is excited by an ultrashort laser pulse. Spatial overlap including a measurement of the spot sizes on the sample between both laser and X-ray beams is set via steering the laser beam onto the X-ray spot on sample, monitored with an imaging CCD camera.

These laser-pump/X-ray probe experiments at synchrotrons exploit a special electron bunch filling pattern (Fig. 1.4) such as that found at the ALS (Berkeley, USA) or the SLS (Villigen, Switzerland), but other filling modes are convenient,

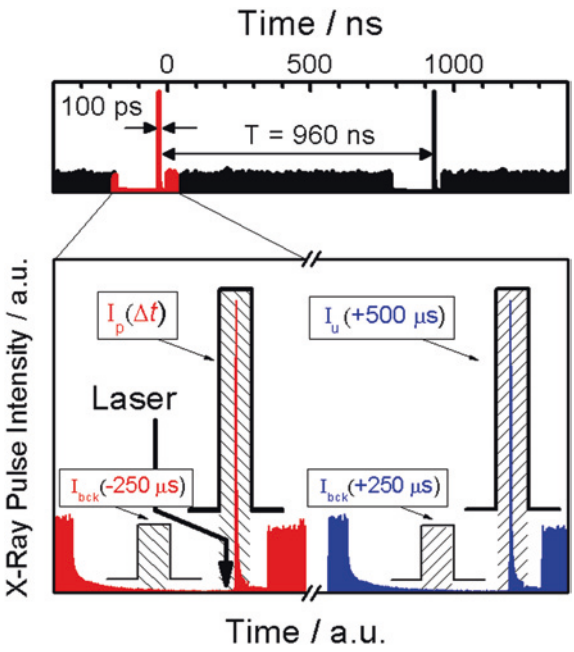

Fig. 1.4 *Top* Typical bunch filling pattern at synchrotrons. Here we show the case of the Swiss *Light Source* Trains of 390 electron bunches with 2 ns spacing are followed by a 180 ns long empty section, in which a densely packed electron bunch (pulse width 100 ps) is placed 30 ns before the start of the bunch train. *Bottom* Data acquisition scheme employed at the microXAS beamline of the Swiss Light Source. A gated integrator measures sequentially the X-ray intensity at the chosen time delay Δt, a background signal ca. 250 μs earlier and later, the X-ray signal of the unexcited sample after 500 μs (each within the indicated shaded time windows). This acquisition scheme is repeated for several thousand times per data point

such as that used at the Advanced Photon Source (APS, Argonne), provided individual pulses can be isolated.

For example, the SLS storage ring consists of 480 so-called buckets, each separated by 2 ns, in which 390 are filled (a filled bucket is also called an electron bunch), while in the subsequent 180 ns dark section a single densely packed (with up to 5 times more charge) hybrid electron bunch is placed. The X-ray pulse emitted from this electron bunch is used to probe the photoinduced changes of the X-ray absorption within the sample. In most experiments so far carried out, amplified laser systems running at 1 kHz were used for photoexcitation, and are synchronized to the round trip frequency of the electron bunch (T = 960 ns at the SLS), thus ensuring a constant time delay between the laser and selected probing X-ray pulses. A gated integrator delivers a sequence of output signals proportional to the input signal integrated over a fixed time window (Fig. 1.4). These signals are recorded with an ADC card, triggered at 4 kHz, to provide a sequence of the X-ray signals when the laser is on and off, but also for recording the electronic background signal with no X-rays present. First, the X-ray signal at time Δt

after laser excitation is measured (I_p), then a background signal without X-rays is recorded after ca. 250 μs (I_{bck}(250 μs)), which enables post-correcting baseline drifts in the gated integrator, and finally, after 0.5 ms, the X-ray signal from a fresh sample without laser excitation is recorded (I_u) followed by a baseline correction measurement (I_{bck}(500 μs + 250 μs), not shown in the figure) [93, 110]. The pump-probe signal in transmission is defined as the transient absorption T_{tr} of the photoexcited sample via [93, 110].

$$T_{tr}(E, \Delta t) = \ln\left(\frac{I_{pum}}{I_{unp}}\right) \tag{1.5}$$

with $I_{pum} = I_p(\Delta t) - I_{bck}(\Delta t + 250\ \mu s)$ and $I_{unp} = I_u(500\ \mu s) - I_{bck}(500+250)$ μs being both the baseline (I_{bck}) corrected photoexcited and unexcited X-ray signals, respectively (see Fig. 1.4). The X-ray signals are measured simultaneously in transmission and fluorescence yield modes, using the same data acquisition strategy for all detectors, as shown in Fig. 1.4. We define the transient signal in fluorescence mode T_{fl} via

$$T_{fl}(E, \Delta t) = \frac{I^{fl}_{pum} - I^{fl}_{unp}}{I_0} \tag{1.6}$$

with I^{fl}_{pum}, I^{fl}_{unp} and I_0 being each baseline corrected as described above for transmission mode. Likewise, normalization of the unpumped spectra to the incident flux yields the static spectrum of the sample.

This data acquisition scheme allows measuring the corresponding signals for every single incident X-ray pulse, and for each data point (e.g., during an energy scan) a few thousand single X-ray pulse intensities are analyzed in order to store the average value and its standard deviation into the computer. This methodology: (i) eliminates drifts due to deterioration of the sample under laser and/or X-ray irradiation (for limited sample volumes), as well as drifts of the X-ray flux; (ii) allows measurements at the shot noise of the X-ray source, implying that changes as low as 10^{-4} X-ray transmission changes can be recorded within a reasonable (typ. 1 s) data acquisition time.

While the above scheme was implemented with 1 kHz repetition rate pump lasers, taking advantage of the high pulse energies available from commercially available amplified laser systems (>1 mJ/pulse), synchrotron X-ray pulses are generally delivered at MHz repetition rates by the storage ring. This implies means that typically 10^3 X-ray pulses are unused. This reduced X-ray flux is a major limiting factor on the achievable signal-to-noise ratio (S/N) of the experiments, which not only reduces the accuracy of the structural analysis but also restricts the types of samples that can be measured to those with a solubility in the range of tens to hundreds of mM, which is not convenient for biological samples. The idea would therefore be to use a pump laser that runs at say, half the repetition rate of the synchrotron but with a large enough energy/pulse to ensure a comparable photolysis yield as in the 1 kHz configuration.

Previous attempts to implement a high-repetition rate pump-probe scheme at synchrotrons were made by Widdra et al. [111, 112] who used a ps laser system operating at 1.25 MHz to match the single-bunch repetition rate at the BESSY synchrotron (Berlin, Germany) for time-resolved core-level photoemission studies of surfaces. Stern et al. [113, 114] used an amplified laser system operating at 272 kHz at the APS to study laser-induced melting of Germanium films. The disadvantage of using high repetition rate excitation with solid samples is the sample damage resulting from the high average power. However, for liquid solutions, high repetition rate excitation is ideal since the flowing sample is continuously refreshed. The Lausanne group recently implemented such an experiment at the SLS using a picosecond high-average power Nd:YVO4 laser operating at variable repetition rate (50 kHz–8 MHz), and producing 10 ps pulses. This product is primarily aimed at industrial users meaning turnkey operation and long-term stability, which are ideal in the environment of a synchrotron. It delivers two orders of magnitude less energy/pulse than 1 kHz amplified femtosecond systems, but the fluence can be identical by tighter focusing of the laser beam. When operated at half the repetition rate of the isolated camshaft pulse of the SLS (520 kHz) this results in 28 μJ/pulse at the fundamental wavelength, 1064 nm. By frequency doubling and tripling one obtains 15 μJ/pulse at 532 nm and 6 μJ/pulse at 355 nm. It is also possible to frequency double the 532 nm light to obtain 266 nm light. The data acquisition scheme is identical to the one described above, with the important difference that the data acquisition rate is increased to 2 MHz. More details are given in [115].

Until recently, most time-resolved XAS studies concerned the hard X-ray range, which is convenient for probing the K-edges of $Z > 18$ elements and the L-edges of $Z > 40$ elements. However, working in the soft X-ray range offers a number of advantages: (a) one could access the K-edges of light elements such as C, N, O, S, etc., which are important for biology; (b) the $L_{2,3}$ edges (due to $2p_{1/2,3/2} \rightarrow 3d$ transitions) of most transition metals are accessed; (c) The smaller intrinsic core hole lifetime width (0.5 eV) of p orbitals results in sharper bound–bound core to valence transitions than K edge ($1\,s \rightarrow 3d$) ones; (d) $2p_{1/2,3/2} \rightarrow 3d$ transitions are dipole-allowed, yielding more intense and more structured spectra than the dipole-forbidden K edge 1 s-3d transitions; (e) the $L_{2,3}$ edge features are directly proportional to the amount of d character of unoccupied or partially occupied valence orbitals of the metal; (f) ligand field multiplet theory [86, 87, 116] is a well-established tool to interpret L edge spectra, delivering a detailed description of the electronic structure.

However, due to the large absorption cross section of solvents and air (e.g., at the Fe L edge energy range the X-ray path length in water is only 1–2 μm) the implementation of soft-X-ray absorption spectroscopy for the study of liquid solutions under vacuum took some time, but is now no longer a problem. Indeed, two strategies have appeared in the last ten to twenty years: (a) the use of cells equipped with soft X-ray transparent windows, such as silicon nitride thin membranes (100–200 nm-thick) [117]; (b) the implementation of the liquid microjet technology, which consists in injecting a liquid jet (typically ≥ 10 μm diameter) at high speed (typically 100 m/s) into the vacuum chamber with a pressure in

the order of 10^{-5} bar [118]. The development of ps and fs soft X-ray absorption spectroscopy is very recent and has made use of the first scheme based on SiN-equipped cells [37, 38, 119, 120].

1.4 Applications

The first time-resolved X-ray experiment used X-ray absorption spectroscopy (XAS) to probe the photoinduced changes in carboxymyoglobin in solution with μsec resolution [121]. Later, Wilson and co-workers [97] used 1.5–3 ps X-ray pulses from a plasma source to probe the disappearance of a shape resonance at the K-edge (2.5 keV) of sulphur upon photodissociation of the SF_6 molecule in the gas phase. Chen and co-workers reported the first study of a molecular system in solution, investigating the photodissociation of ligands from [Ni(tpp)L_2] (Ni(tpp) = Nickel(ii) tetraphenylporphyrin and L = axial piperidine ligand, which was also the solvent in their study), and their recoordination with 14 ns resolution using synchrotron X-ray pulses. They addressed the issue as to whether the recoordination process is a concerted or a sequential (two-step recombination with [Ni(tpp)L] as an intermediate) process, concluding that the process is concerted on the time scale of their resolution.

Time resolved XAS studies of molecular systems in solution really took off in the first half of the 2000s. Most of these have been transition metal molecular complexes, for obvious technical reason as the methodology was first implemented in the hard X-ray range where it is possible to carry out the experiments in air or under a gas atmosphere. In addition, metal-based molecular complexes, such as metalloporphyrins, haems or chlorophylls, are heavily involved in natural processes involving energy and electron transfer, such as photosynthesis, oxygen transportation, [122, 123] etc., and in applications such as functional molecular devices [124, 125], solar energy, molecular electronics, sensitizers, photocatalysis, etc. Below we give a number of processes occurring in these systems, which have been investigated by time-resolved XAS both in the hard and more recently, in the soft X-ray range.

1.4.1 Intramolecular Charge Transfer

Controlled electron transfer (ET) and charge separation in molecular assemblies are essential requirements for efficient storage and conversion of energy by chemical means. In most light-induced processes in metal-based molecular complexes, the doorway states to excitation are the metal-to-ligand-charge-transfer (MLCT) states, whose absorption bands dominate the visible absorption spectrum. Because a charge is transferred within a molecule there is a significant change of the field of forces within the molecule, but also a dipole moment change. Therefore in solutions, there are issues of both intramolecular and subsequent intermolecular (i.e. solvent)

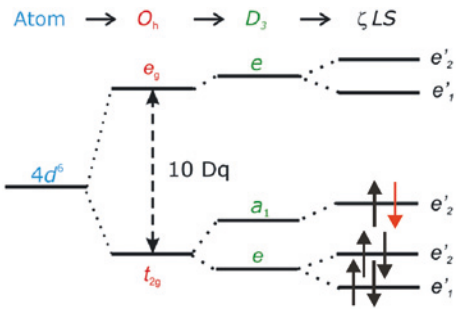

Fig. 1.5 Energy level scheme for a $4d^6$ transition metal complexes such as $M(bpy)_3$, with M = Ru, Fe. The atomic 4d orbital splits into a 6-fold degenerate t_{2g} and a 4-fold degenerate e_g. level in the octahedral field of the ligand (separated by 10Dq). Trigonal distortion due to the D_3 symmetry of the complex partial lifts the degeneracy, which is further lifted into 5 two-fold degenerate levels by the 4d spin–orbit coupling. The electron occupancy of the ground state (completely filled in t_{2g}, and empty for e_g) is indicated by the arrows, one (in *red*) is removed to the bpy ligand following photoexcitation of the metal-to-ligand-charge-transfer (MLCT) states

structural rearrangements as a result of the electron transfer. Such processes have been investigated on ruthenium and copper complexes, as described below.

The Lausanne group carried out a picosecond $L_{2,3}$-edge XAS study of aqueous Ruthenium(II)-tris-2,2′-bipyridine ($[Ru^{II}(bpy)_3]$) [88, 126]. In the predominantly octahedral field of the complex, the d-orbitals split into a lower t_{2g} orbital and an upper e_g orbital (Fig. 1.5).

These are further split by the addition of the trigonal distortion and by the spin–orbit interaction. Fig. 1.6 shows the ground state (a) and transient XAS (b) spectra, next to the extracted excited state XAS (c). In the ground state, all six 4*d* electrons are in the lower t_{2g} orbital while the e_g orbital is empty, and therefore only the B band ($2p \rightarrow 4d(e_g)$) appears. In the MLCT state, an electron is transferred to the bpy ligand, thus opening up a new transition ($2p \rightarrow 4d(t_{2g})$, feature *A*′). In room temperature aqueous solutions, the ^{3}MLCT state exhibits a measured lifetime of about 600 ns [127]. Also, the blue-shift of the *B* feature reflects the change of oxidation state, in good agreement with previous experimental and theoretical work [128, 129].

The XANES region was analyzed by the ligand field multiplet theory, [88] in very good agreement with the data (see Fig. 1.6d). From the change of ligand field splitting between ground and excited state and using an electrostatic model that relates the octahedral ligand field splitting to the metal–ligand distance, [130] a Ru–N bond contraction of ~0.02 Å in the excited state was derived, while the analysis of the EXAFS region [64] (D, D' features) delivers a value of the Ru–N bond contraction of -0.037 ± 0.0135 Å, treating all Ru–N distances equally (i.e., in D_3 symmetry). This relatively weak bond contraction, despite a dramatic change of the electronic structure, results from steric effects because the three byp ligands are already in a constrained geometry in the ground state. Our results were later confirmed by Quantum chemical calculations of the ^{3}MLCT structure by Nozaki et al. [131] and Alary et al. [132].

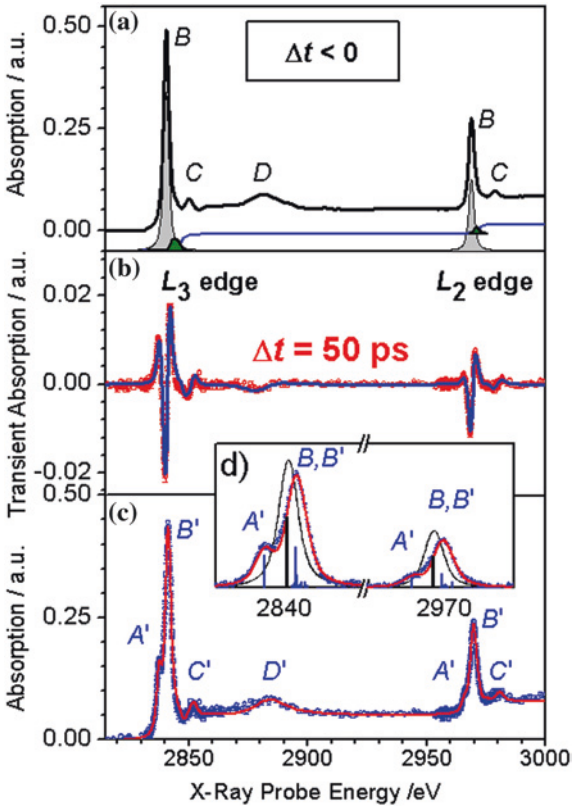

Fig. 1.6 **a** $L_{2,3}$ edge XAS spectrum of aqueous $[Ru^{II}(bpy)_3]^{2+}$ in its ground state (*thick black line*) together with fits of its most prominent features (labeled), except for the two residual bands (*green areas*) near the ionization potential. The edge step functions for IP for each state is shown as well (*blue line*). See [88] for details of the fit. **b** Transient absorption spectrum (*open red circles* with error bars) and a fit of this transient (*blue line*) using the ground state spectrum and the (energy-shifted) decomposed bands shown in **a**. **c** Reconstructed XAS of the ^{3}MLCT state (*blue data points*) together with a fit to the most prominent features. **d** The A(A′) and B(B′) features extracted from the spectrum after subtraction of the edge step and the higher-lying weak bound–bound absorptions shown in **a**, and compared to multiplet calculations. The sticks (thick for the ground state and thin for the excited state) are the transitions which are broadened with the Gaussian and Lorentzian widths due to experimental resolution and lifetime width, to generate the solid (*red*) curves

In another example of structural changes due to intramolecular electron transfer processes, Chen et al. [133] investigated the structure of the MLCT states of Cu(I)-diimine complexes ($[Cu^I(dmp)_2]^+$ (dmp = 2,9-dimethyl-1,10-phenanthroline)) by ps XAS. Upon 400 nm photoexcitation of the system one reaches the S_2 state, which decays on an ultrafast time scale to the S_1 state [133–136] that then relaxes to the T_1 state (Fig. 1.7a). In these processes, the system changes from a tetrahedral geometry to a flattened one (Fig. 1.7b).

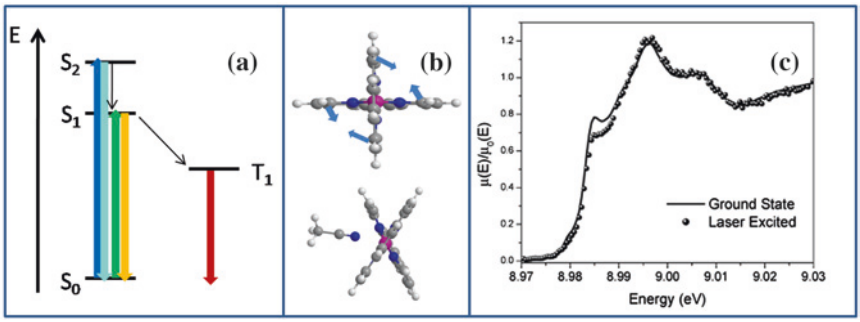

Fig. 1.7 Photocycle of cooper(I)-diimine complexes: upon excitation of the S_2 MLCT state the system changes from Cu(I) to Cu(II) and an ultrafast internal S_2-S_1 conversion occurs (**a**). In this step, a geometry change towards a flattening occurs (**b**), which is thought to take place in the S_1 state prior to intersystem crossing to the T_1 state [133, 134, 208]. The latter has a ns lifetime so that it can be probed by ps XAS as done in refs. [136, 209] (**c**)

Chen et al. observed the photoinduced electronic and structural changes by ps XANES and EXAFS (Fig. 1.7c) and found that: (1) the excitation of the MLCT state transition induces an electronic configuration change from Cu^{I} ($3d^{10}$) to Cu^{II} ($3d^{9}$); (2) the inner-sphere reorganization changed the coordination number of the MLCT state from four to five in toluene, which is presumed to be non-coordinating; (3) the average Cu-ligand bond lengths increased in the MLCT state in toluene, but decreased in acetonitrile, reflecting the difference in the interactions of the copper with the fifth ligand. These conclusions were further supported by simulations of the XANES part of the spectra [137]. In the meantime, we have carried out ps XAS measurements in similar complexes and complemented them by Quantum Mechanics/Molecular Mechanics molecular dynamics simulations, and came to the conclusion that there is no coordination of a solvent molecule to the Cu atom [138]. Nevertheless, questions still remain open as to the sub-ps dynamics, which may be addressed by fs XAS in the future.

1.4.2 Bond Formation in Bimetallic Complexes

The triplet excited states of dinuclear d^8--d^8 platinum, rhodium, and iridium complexes (bridged by various ligands) exhibit remarkable photophysical and photochemical properties, which are strongly determined by their structure [140]. The unusually high photocatalytic activity of these complexes are a manifestation of the newly formed bond in the lowest excited singlet and triplet $^{1,3}A_{2u}$ states, owing to the promotion of an electron from the antibonding $d\sigma^*$ (d_z^2-derived) to the bonding $p\sigma$ (p_z-derived) orbitals, which should therefore lead to a contraction of the metal–metal bond (Fig. 1.8).

The $[Pt_2(P_2O_5H_2)_4]^{4-}$ molecule is among the most extensively studied d^8--d^8 dinuclear metal complexes. In solutions, excitation into the first singlet state in

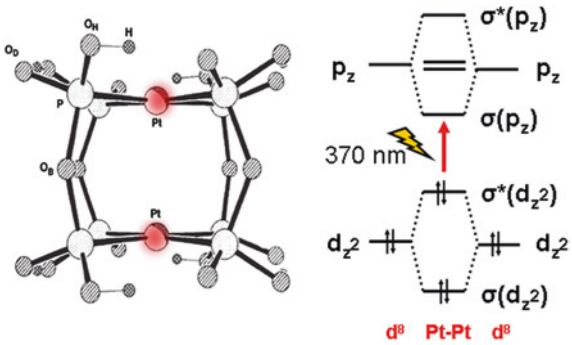

Fig. 1.8 Structure of the $[Pt_2(P_2O_5H_2)_4]^{4-}$ molecule (*left*). The maximum of the first singlet absorption lies at 370 nm. Excitation of a d^8–d^8 complex promotes an electron from the antibonding dσ* (d_z^2-derived) to the bonding pσ (p_z-derived) orbitals, leading to formation of the Pt–Pt bond and contraction of its distance in the excited state

the near UV region around 370 nm leads to formation of the long lived (~1 μs) triplet state with unity quantum yield. van der Veen et al. [141] resolved its structure by picosecond EXAFS. Figure 1.9a shows the ground state Pt L_3-edge XAS spectrum (black trace) as well as the transient spectrum, integrated from 0 to 150 ns to improve the signal-to-noise ratio. The inset shows the XANES region for the ground-state complex and its transient spectrum, wherein dramatic changes appear. In particular, a new absorption shows up at 11.574 keV below the absorption edge, which is due to the creation of a hole in the 5dσ* orbital upon laser excitation, which can then be accessed from the $2p_{3/2}$ core orbital (L_3 edge). Clear changes are visible in the EXAFS region (Fig. 1.9b), reflecting structural modifications between the ground and excited triplet states.

From the transient EXAFS spectrum (Fig. 1.9b), the magnitude of the Pt–Pt bond contraction as well as, for the first time, the changes affecting the Pt–P bonds were extracted, [141] and the best fit is shown in Fig. 1.9b. It was found that while the Pt–Pt bond contracts by 0.31(5) Å, in very good agreement with the X-ray photocrystallography data [142], it was shown that Pt–P bonds slightly elongate (by ~20 mÅ) in agreement with theoretical predictions [142]. This work underscores the ability to retrieve details of the excited state structure of a rather complex molecular system in liquid solution, due to the high sensitivity of the experiment, coupled to a rigorous structural analysis based on fitting the transient EXAFS spectra directly in energy space [83]. Almost simultaneously to the work by van der Veen et al. [141], Christensen et al. [27] reported a picosecond solution X-ray scattering study of the same system, deriving a somewhat similar contraction of the Pt–Pt bond. More recently, Chen and co-workers [143] reported on ps XAS studies of another diplatinum complex, which also produced rather similar results.

Pt_2POP is a remarkable molecule in the sense that its ground and excited potentials are highly harmonic and that the optical spectrum is only sensitive to the Pt–Pt coordinate. It is therefore easy to retrieve the excited state structure from a Franck–Condon analysis, which shows a Pt–Pt bond contraction in the triplet

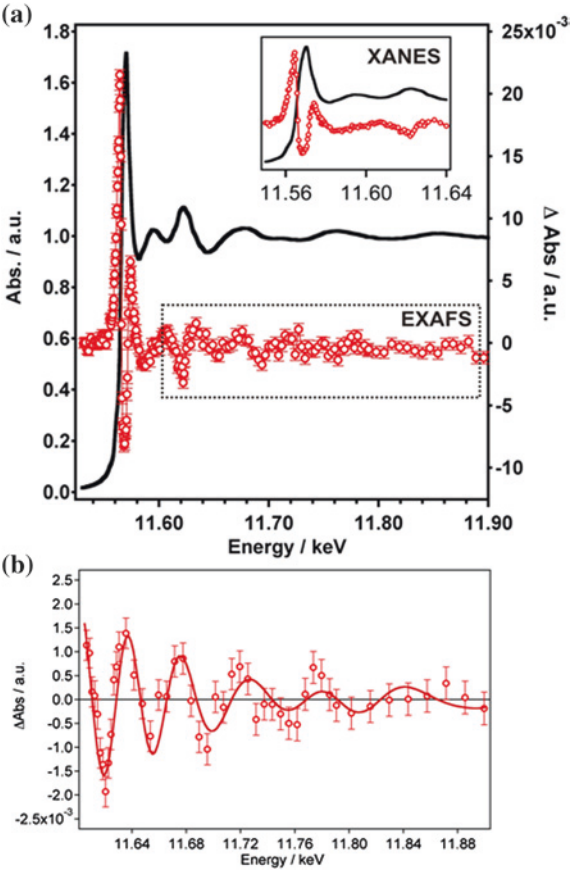

Fig. 1.9 **a** Static Pt L_3 XAS spectrum of $[Pt_2(P_2O_5H_2)_4]^{4-}$ in solution (*black line*, *left* axis) and the transient (excited–unexcited) XAS spectrum (*red circles*, *right* axis, same units as *left*) integrated up to 150 ns after excitation. The inset zooms into the XANES *region*. **b** Transient EXAFS data and best fit (*solid line*) with the following results: a Pt–Pt contraction of 0.31(5) Å, a Pt-ligand elongation of 0.010(6) Å, zero energy shift and 7 % excitation yield. The best-fit structural distortions are indicated in the upper right corner (see [141, 206] for details)

state 0.1 Å smaller than that derived in [141–144]. The origin of the discrepancy lies, we believe, in the fact that the EXAFS analysis neglected the contribution of the solvent, while the optical domain spectroscopy is not sensitive to it. This shows that solvent contributions have to be included in the analysis of EXAFS and XANES, which opens a new level of refinement in the structural determination. Work is in progress towards such refinements. A recent paper reports on such calculations and show a clear contribution of the solvent in the signals [139].

1.4.3 Spin Cross-over in Fe(II)-Complexes

One of the fascinating features of Fe^{2+} or Fe^{3+} metal-based molecular complexes is their ability to change spin under temperature, pressure or light irradiation and they have therefore been named spin cross-over complexes (SCO) [145]. In the

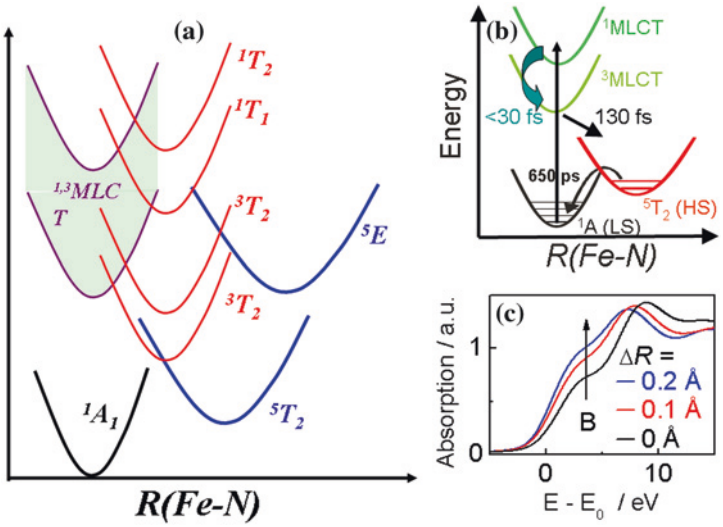

Fig. 1.10 **a** Typical potential energy curves of Fe(II)-complexes as a function of the Fe–N bond distance adapted from [146]. The manifold of metal-to-ligand-charge-transfer (MLCT) states is shown as a shaded area. $[Fe^{II}(bpy)_3]^{2+}$ has a predominantly O_h symmetry with a trigonal (D_3) distortion. The metal-centred (MC) states are represented by their symmetry character (A, T and E) in the D_3 group. In the latter, the LS $^1A_1$ ground state has a completely filled $e^4a_1^2$ configuration (deriving from the t_{2g}^6 subshell in O_h symmetry), while the antibonding e (e.g. in O_h symmetry) orbital is empty. Per electron promoted from the t_{2g} to the e.g. subshell (for easier reading we will use from here on the O_h nomenclature) the metal–ligand bond length increases by as much as 0.1 Å [146]. For the series of $^{1,3}T(t_{2g}^5e_g)$ states, it is expected to be in between the ground and the high-spin $^5T_2$ ($t_{2g}^4e_g^2$) state. **b** Relaxation cascade as determined by ultrafast laser spectroscopy upon excitation of aqueous $[Fe(bpy)_3]^{2+}$ at 400 nm [156]. The intermediate MC states are not shown as they are optically silent in the UV–Visible and were therefore not observeable. **c** Simulated XANES spectra for different Fe–N bond elongations from the ground state equilibrium value of 1.97 Å, using the MXAN code [91]. The elongations correspond to the ground and the MLCT states (0 Å), the intermediate ligand field $^{1,3}T$ states (0.1 Å) and the ^5T state (0.2 Å). The horizontal axis is given as energy from the ionization potential

predominantly octahedral field due to the ligands (Fig. 1.5), all electrons are in the lower t_{2g} sub-shell in the low spin (LS) ground state, while transferring electrons to the e.g. orbitals increases the spin state. Because the e.g. orbitals derive from the $d_{x\text{-}y}^{22}$ and d_z^2 orbitals, they are antibonding in 6-fold coordinated complexes, which leads to a striking metal–ligand bond elongation in the high spin (HS) state. A generic diagramme of the potential energy curves of the various states of Fe(II)-based complexes is shown in Fig. 1.10a, as a function of the Fe–N bond length [146]. The MLCT states have nearly the same equilibrium distance as the ground state, in agreement with [88], the ligand field states $^{1,3}T$, ^5T and ^5E have their equilibrium distances elongated by ~0.1, ~0.2 and ~0.3 Å, respectively, relative to the ground state bond distance. Light excitation into the singlet Metal-to-Ligand-Charge-Transfer (^{1}MLCT) state or to the lower-lying ligand field states leads to

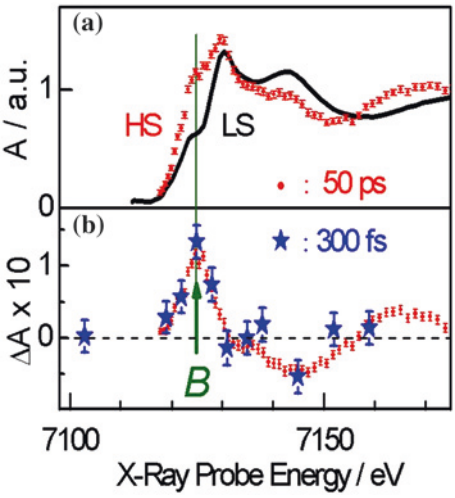

Fig. 1.11 **a** XANES spectrum of the LS state of $[Fe^{II}(bpy)_3]^{2+}$ (*black*) and the HS state (*red points*). The latter is extracted from the difference spectrum (shown in **b**) and the LS spectrum, based on the prior determination of the fraction of excited molecules. **b** Difference transient spectrum at 50 ps time delay (*red points*), and at 300 fs (*blue stars*) obtained with the slicing scheme

population of the lowest quintet state $^5T_2$ with unity quantum yield [145]. The lifetime of the latter varies by several orders of magnitude as a function of ligand and temperature [145] with $[Fe^{II}(bpy)_3]$ having the shortest lived quintet state lifetime (650 ps) at room temperature.

Structural studies by X-ray diffraction or X-ray absorption spectroscopy under quasi steady-state conditions, pointed to a bond elongation of ~0.2 Å of the Fe–N bond for Fe(II)-based complexes with long-lived HS states [147–149] but the question arose if this applies to the shortest lived HS state of $[Fe^{II}(bpy)_3]$, as predicted by theory [150].

Khalil et al. [151] and Gawelda et al. [152] captured the structure of the quintet state after laser excitation using 70 ps hard X-ray pulses probing the structure changes at the K edge of Iron. In the first case, the system was $[Fe^{II}(tren(py))_3]$ in acetonitrile, which has a quintet state lifetime of 60 ns, while the second case was $[Fe^{II}(bpy)_3]$, which we describe in more details now. Figure 1.11 shows the Fe *K*-edge XANES of the molecule in the ground state, the transient (difference) spectrum at 50 ps time delay and the XAS spectrum of the quintet state, as retrieved from the ground state and the difference spectra and from the photolysis yield determined in laser-only experiments (and convoluted to match the much longer X-ray probe width). The structural analysis of the excited state was based on fitting both the transient XANES [152] and the transient EXAFS spectra [58, 83] in energy space. These deliver the same Fe–N bond elongation $\Delta R_{Fe\text{-}N} = 0.20$ Å, but the precision increased considerably using the latter procedure (0.203 ± 0.008 Å).

The fact that the bond elongation is nearly the same in the HS state in all complexes, regardless of its lifetime [147, 151] implies that the bond elongation is not the parameter that controls the decay rate of the quintet state to the ground state. Rather, the adiabatic energy and the coupling parameters between low spin and

high spin state are the crucial parameters. Indeed, of all Fe(II)-SCO complexes, $[Fe^{II}(bpy)_3]^{2+}$ has the highest lying quintet state.

In order to describe the electronic structure of the quintet state, Huse et al. [120] carried out picosecond L-edge spectroscopy of $[Fe^{II}(tren(py))_3]$. This experiment was the first of its sort and it used a liquid cell equipped with SiN membrane windows. Their results showed a significant reduction in orbital overlap between the central Fe(3d) and the ligand N(2p) orbitals, consistent with the expected ~0.2 Å increase in Fe–N bond length upon formation of the high-spin state. The overall occupancy of the Fe(3d) orbitals remains constant upon spin cross-over, suggesting that the reduction in σ-donation is compensated by significant attenuation of π-back-bonding in the metal–ligand interactions. These results show the power of ps soft X-ray spectroscopy to fully unravel the details of the electronic structure of the systems under study, and its complementarity with hard X-ray spectroscopy.

Femtosecond resolution in X-ray absorption spectroscopy is however needed if one wants to follow the ultrafast structural dynamics of photoexcited systems in real-time, and thus answer a host of questions that have escaped femtosecond optical spectroscopies or ps XAS. Femtosecond XAS was recently implemented in the hard and the soft X-ray ranges to fully resolve the photocycle of the above spin cross-over systems.

Indeed, the mechanism and relaxation pathways of the photoinduced HS-LS conversion in Fe(II) complexes were still unknown, and in particular the pathway leading from the initially excited ^{1}MLCT state to the lowest lying excited quintet state [145, 153, 154]. One of the reasons for this situation was the fact that the intermediate ^{1,3}T state (Fig. 1.10a) are optically silent, while the HS quintet state absorbs below 320 nm [155]. The early time dynamics was identified by Gawelda et al. on $[Fe^{II}(bpy)_3]$ in laser-only studies, [156] who found that departure from the ^{3}MLCT state occurs in ~130 fs (Fig. 1.10b). The XANES spectrum of the ground state (Fig. 1.11) shows a shoulder (the B-feature) on the edge, which is a multiple scattering feature [157]. Upon Fe–N bond elongation in the quintet state its intensity increases causing the significant peak at low energy in the transient spectrum (Fig. 1.11b). Simulations based on multiple scattering theories confirm the distance dependence of the B-feature (Fig. 1.10c), which one can use to identify the various electronic states possibly involved in the relaxation cascade.

Using hard X-ray fs pulses generated by the slicing scheme at the SLS, Bressler et al. carried out an optical pump/X-ray probe experiment following the evolution of the B-feature as a function of pump-probe delay. Figure 1.12 shows the time scan obtained at the B-feature (7.122 keV) showing that the signal stabilizes from about 300 fs up to the scan limit of 10 ps (see inset), which is evidence that the system is already in the quintet state. Further evidence is the energy scan at 300 fs, which reproduces the transient spectrum at 50 ps time resolution (Fig. 1.11b). The fit in Fig. 1.12 shows that the quintet state is reached in 150 ± 50 fs. This time corresponds to the decay of the ^{3}MLCT state, implying that the ultrafast spin conversion is a simple three-step ^{1}MLCT - ^{3}MLCT - $^5T_2$ cascade that bypasses the intermediate ^{1,3}T states.

The time scale of ~150 fs corresponds to about two oscillations of the Fe–N stretch vibration [158], suggesting a nearly non-Born–Oppenheimer process. This

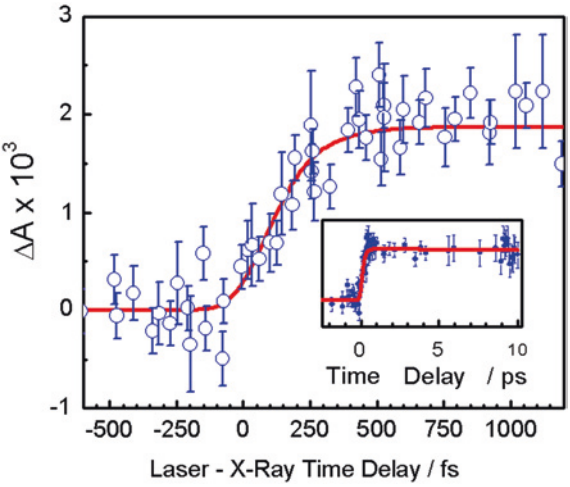

Fig. 1.12 Time scan of the signal (*blue points*) at the B-feature (Fig. 1.6c), as a function of laser pump/X-ray probe time delay after excitation of aqueous $[Fe^{II}(bpy)_3]^{2+}$ at 400 nm. The inset shows a long time scan up to 10 ps time delay. The *red trace* is the simulated signal assuming a simple 4-step kinetic model $^1A_1 \rightarrow {}^1MLCT \rightarrow {}^3MLCT \rightarrow {}^5T$ to describe the spin conversion process. The vertical arrow displays the expected absorption increase for an elongation of 0.2 Å for the Fe–N distance ΔR between the LS and HS states (see Fig. 1.10c)

experiment illustrates the power of ultrafast XAS to retrieve dynamical information difficult to obtain by laser-only experiments. It also shows how structural dynamics studies can identify the electronic relaxation pathways of complex molecules, while so far the opposite was common practice. Further visible pump/UV probe transient experiments of the quintet state identified its vibrational relaxation dynamics, [159] thus providing a complete picture of the photocycle of aqueous $[Fe^{II}(bpy)_3]$. A full description of the combined optical and X-ray studies on this system is given in a recent review [160].

Very recently, Huse et al. [38] carried out the first time femtosecond soft X-ray experiment of a similar spin cross-over molecular system in solution, which fully confirm the above results. Their experiment represents a real breakthrough as it demonstrated the visualization of ultrafast electronic structure changes of dilute molecular systems in solution by soft XAS.

1.4.4 Dynamics of Pure Water

The unusual properties of water have stirred much research. Liquid water can be regarded as a highly dynamic network of molecules connected through hydrogen bonds. The results of static X-ray absorption spectroscopy measurements show a pre-edge peak (I) followed by a main-edge (II) and a postedge feature

(III) related to local water structures with specific coordination and hydrogen bonding. There has been much controversy over the correct structural model and their relative merits in determining the average number of hydrogen bonds per water molecule [117]. Nevertheless, there is consensus on a qualitative level as to the structural meaning of the three characteristic spectral regions of the oxygen K-edge and how these features change upon melting of ice as well as heating of liquid water. In order to describe how the different structures interchange upon heating of water, Huse et al. [161] and Wernet and co-workers [119, 162] demonstrated infrared pump/soft X-ray probe investigation of pure water at the K edge of Oxygen. However, the tens of ps time resolution of these experiments precluded observations at relevant time scales. Therefore, Wen et al. [37] extended these experiments to the femtosecond range using the slicing scheme at the ALS. They recorded the conversion of highly coordinated water structures to less-ordered structures with weaker hydrogen-bonding via fs-XANES spectroscopy upon vibrational excitation, exploiting the relation between coordination/order and distinct X-ray spectral features due to the high sensitivity of XANES regions to chemical coordination. The observed dynamics was described by a 0.7 ps thermalization time that is characteristic of the hydrogen bond network in water. Their transients capture the formation of a high-pressure phase distinct from the equilibrium state of liquid water.

This work was the first femtosecond soft X-ray study of a liquid-phase system. It demonstrated the feasibility and prospects of solution-phase ultrafast X-ray studies in the soft X-ray range where K-edges of C, N, O and L-edges of transition metals deliver chemically specific information about coordination, valence charges distribution, bonding and atomic structure in order to uniquely follow chemical reactions and solvation dynamics on ultrafast time scales. As a matter of fact, the same team demonstrated ps and fs soft X-ray spectroscopy at the L edge of Fe in an SCO complex as discussed above ([38, 120]) and at the N K-edge of photoexcited $[Fe^{II}(bpy)_3]$, [120].

1.4.5 Solvation Dynamics and Hydrophobicity

The above examples on Copper, Platinum and Ruthenium complexes alluded to the role of the solvent in the photoinduced structural changes. Electronic solvation dynamics is the rearrangement of the solvent molecules around a solute as a result of an electronic redistribution in the latter. This electronic redistribution may be caused by photoexcitation or simply by a chemical reaction. The role of the solvent is crucial in enhancing or hindering reactions, via its modification of barriers and the dynamics of solvation is intimately influenced by the intramolecular dynamics. So far solvation dynamics has only been investigated by ultrafast optical techniques (transient absorption or fluorescence up-conversion), [163–165] which do not deliver structural information. In these studies a dye molecule is excited in a solvent, inducing either a dramatic dipole moment change

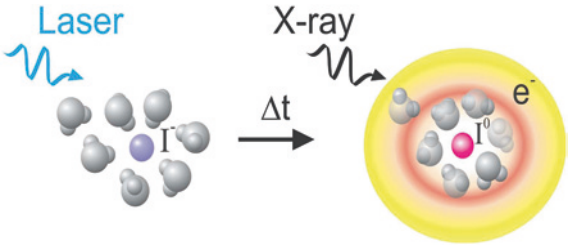

Fig. 1.13 Principle of the optical pump/X-ray probe experiment on solvation dynamics. The electron of the iodide (isoelectronic with Xe) is removed by an ultrashort laser pulse. The evolution of the structural changes in the solvation shell is probed by an X-ray pulse that records the changes at the iodine L edges

(polar solvation) or an expansion of the electronic cloud (non-polar solvation) in such a way that depending on the polar or non-polar nature of the solvent, respectively, a dramatic solvent shell reorganisation occurs, which minimises the free energy. While this approach delivers detailed information about the dynamics of the system, the solvent shell structure cannot be recovered. In addition, the solvent rearrangement depends on the shape and size of the molecule in the ground state. In order to capture the solvent structural dynamics and to obtain a general description of the solvation dynamics, we carried out time-resolved XAS studies of the solvent rearrangement around photoexcited aqueous iodide. In this case, the UV (<260 nm) photoexcitation abstracts the electron from the iodide, leaving a neutral iodine behind (Fig. 1.13) and the solvated electron. It turns out that this changes the solute from a hydrophilic one to a hydrophobic one.

Hydrophobicity is considered the major driving force behind fundamental biological and chemical processes. In the hydration of small hydrophobic species, the formation of small cavities in the solvent to accommodate the solute is an entropically dominated process, and the presence of the solute constrains the orientational and translational degrees of freedom of the neighbouring water molecules. The microscopic understanding of hydrophobic hydration relies so far almost solely on theory and simulations, due the fact that experimentally probing hydrophobicity at the atomic scale is very difficult, and quantitative studies are not yet available.

We previously carried out a preliminary picosecond XAS study of multiphoton-excited aqueous iodide, which showed significant changes in the XANES and EXAFS regions of the $L_{1,3}$ edges 50 ps after excitation, suggesting an extensive solvent rearrangement in the transition from iodide to iodine [166]. Soon after, Elles et al. [167] reported a similar study on aqueous bromide excited into the so-called charge-transfer-to-solvent (CTTS) bands by one-photon at 200 nm, and probed the resulting neutral bromine atom was done at its K-edge using picosecond hard X-ray pulses. Their recovered Br^0 K-edge spectrum showed shallow features above the edge, making it difficult to extract a solvent shell structure. For this purpose, they carried out Monte-Carlo simulations of the radial distribution functions (RDF) of Br^- and Br^0, and found that indeed in the latter case,

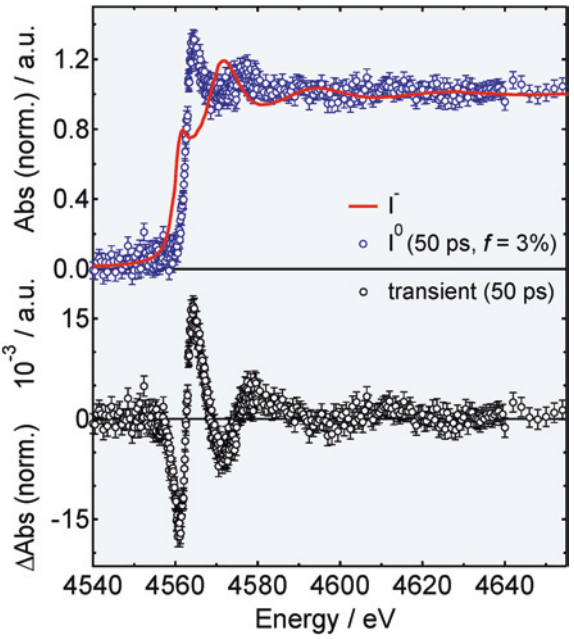

Fig. 1.14 **a** Normalized static iodide L_3 edge XAS (*solid line*) and reconstructed I^0 spectrum using the transient spectrum at 50 ps time delay **b** and the photolysis yield of 3 % (see 39), sample concentration 100 mM; **b** Normalized L_3 edge transient spectrum at a time delays of 50 ps

the solvent shell structure is more diffuse and expands by ~0.5 Å, explaining this way the weak modulations of the spectrum above the Br^0 K-edge. Their RDF also exhibited a small peak at shorter distances, which they attributed to formation of a $Br^0 \ldots OH_2$ charge transfer complex, although no signature of this complex was found in the time-resolved X-ray signal.

Pham et al. [39] recently carried out a detailed ps and fs XAS study of photoexcited aqueous iodide, which was complemented by detailed quantum chemical calculations and molecular dynamics simulations [39]. While the L_1-edge (originating from the 2 s core orbital) informs us about the electronic structure of the systems, in particular via the appearance of the 2 s-5p resonance that becomes possible upon formation of neutral iodine, the L_3 edge (originating from the $2p_{3/2}$ core orbital) is ideal for probing the geometric structure of the solvent shell. Figure 1.14 shows the static L_3 iodide spectrum (solid line in (a)), the transient spectrum (b) and the recovered iodine spectrum (points in (a)). Dramatic changes are observed which point to an extensive rearrangement of the solvent shell. In order to quantify it, we carried out both classical and quantum mechanics/molecular mechanics (QM/MM) molecular dynamics (MD) simulations. The iodide solvent shell had already been described by QM/MM MD simulations, [168] and the resulting RDF is show in Fig. 1.15 for both the I–O and the I–H distances. Figure 1.15 also shows the RDF's obtained by classical and QM/MM MD for iodine. Both types of MD simulations show an increase of the I–O distances from iodide to iodine, but the most dramatic changes show up on the I–H RDF, where the first peak shifts on average by well over 1 Å

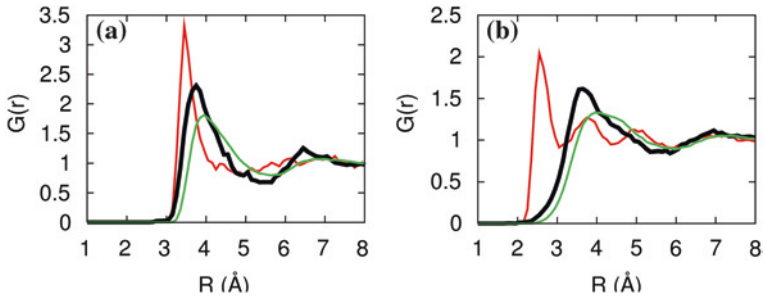

Fig. 1.15 I-O (**a**) and I-H (**b**) radial distribution functions (RDF) of aqueous iodide (*red lines*, same as in [168]) and iodine for the classical MD (*green lines*) and the QM/MM MD (*black lines*). The QM/MM MD simulations represent an equilibration over 15 ps with a single I^-/I^0 described at DFT level of theory. The I^0-O/H RDFs were equilibrated for 10 ns in the CMD simulations

from iodide to iodine. While for iodide the first peak of the I–H RDF lied at smaller distances than that of the I–O RDF, for iodine it is at almost the same distance as the first peak of the I–O RDF, but it is broader and has a long tail extending to larger distances. Finally, the I–H RDF shows clear modulations in the case of iodide, but the separation between solvent shells is less clear cut in the iodine case.

All this indicates that the majority of the hydrogen atoms rotate and point away from the iodine atom, contrary to the iodide case. We used these RDFs to simulate the transient L_3 EXAFS spectrum and both classical and QM/MM MD of neutral iodine delivered a good agreement with the experimental data. The main result is that the experimental data confirms the expansion of the solvent cage from I^- to I^0, with an increase of the cage radius (measured on the I–O distance) of 5–20 % (depending on the type of simulations). Furthermore the RDFs already suggest the formation of a hydrophobic cavity as the water hydrogen atoms prefer now to point towards other water molecules rather than towards the solute.

Sub-picosecond transient XANES spectra are shown in Fig. 1.16 where one can note a broadening on the blue side of the features that appear at the L_1 edge, compared to the 50 ps transient. Based on quantum chemical calculations and QM/MM MD simulations of an $I^0(H_2O)_9$ cluster in bulk classical water, this broadening is caused by the occurrence of a weakly bound and short lived (few ps) I^0-OH_2 complex, whose 2 s-5p resonance is slightly blue shifted compared to that of the uncomplexed Iodine atom due to the formation of a 3-electron bond between iodine and water, therefore causing the observed broadening.

The simulations show that the lifetime of the complex is determined by the time it takes to complete the formation of a cavity of hydrogen bonded molecules around the solute (hydrophobic solvation) following electron abstraction from iodide. This study showed the power of combining ps and fs XAS with high-level quantum calculations and molecular dynamics simulations to unravel the complete dynamics of the system.

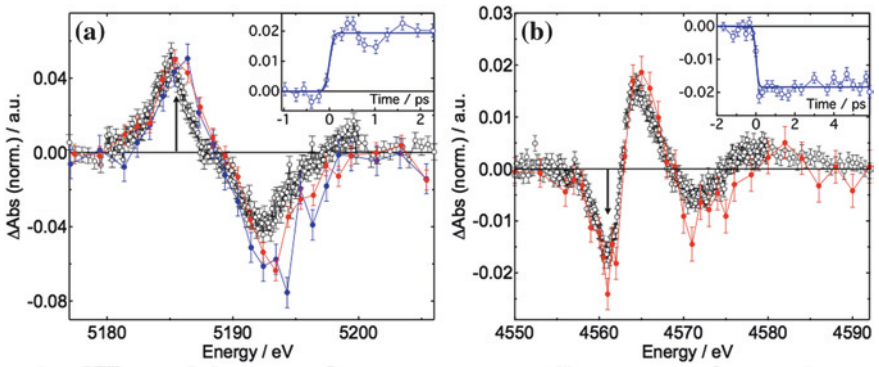

Fig. 1.16 **a** Normalized transient L_1 edge spectrum of photoexcited aqueous iodide at 50 ps (*black dots*), 300 fs (*red dots*) and 850 fs (*blue dots*) time delays after excitation. **b** same as **a** but for the transient L_3 edge spectrum. The sub-ps transients were multiplied by a factor of 1.75 in order to match the value of the 50 ps transient at the maximum of the positive feature. The insets show the time traces recorded with fs resolution at 5185.5 eV **a** and 4561 eV **b**, denoted by arrows, together with their fits by a step function with a rise time of 250 fs corresponding to the cross correlation of the optical and X-ray pulses

1.4.6 Towards Biological Systems

Metalloporphyrins are the basic constituents of a large class of biological systems and play a central role in photosynthesis and in respiration [169]. Time-resolved XAS should solve a number of important questions concerning their relaxation pathways and mechanism after photoexcitation. Indeed, similar to the above presented Iron(II)-polypyridine complexes, metalloporphyrins contain several optically silent metal-centred (or so-called *d–d* states), which can be accessible by XAS.

Chen et al. pioneered the study of metalloporphyrins in solution [55, 59, 170–172]. They first studied the ligand (L) photodissociation of $[Ni(tpp)L_2]$ (Ni(tpp) = Nickel(ii) tetraphenylporphyrin and L = axial piperidine ligand, which was also the solvent in their study), and their recoordination with 14 ns resolution using synchrotron X-ray pulses [171]. The process has a time constant of 28 ns, which is sufficiently long to be resolved. They demonstrated time-resolved XAS measurements for dilutions as low as 1 mM, which are important for biology. They also found that the photodissociation intermediate is square-planar under their time resolution limit. Next, they investigated the structure of the unligated nickeltetramesitylporphyrin ($Ni^{II}TMP$) in the excited triplet state. Here the idea was to resolve the transient electronic structure. Indeed, The electronic configuration of Ni(II) ($3d^8$) in an almost square-planar ground state S_0 has an empty $3dx^2\text{-}y^2$ molecular orbital (MO) and a doubly occupied $3dz^2$ MO. Upon $S_0 \rightarrow S_1$ transition, the S_1 state is believed to decay to an intermediate state T_1' state that then undergoes vibrational relaxation to a relaxed T_1 triplet state, with a presumed

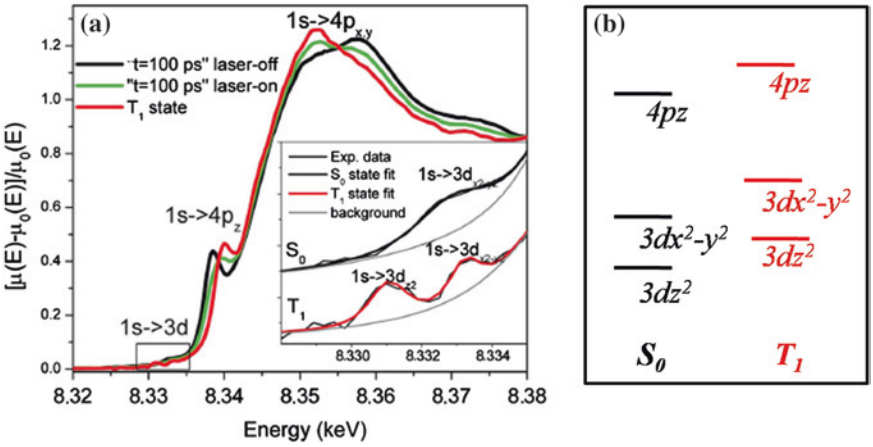

Fig. 1.17 **a** Ni K-edge XANES spectra of NiTMP; inset: pre-edge region. *Black*, laser-on at t = 100 ps; *green*, laser-on at t = 100 ps; and *red*, the T1 state spectrum; t = delay time). The X-ray absorption near-edge structure (XANES) spectra of the Ni K-edge is rotated counter-clockwise by 90° from the conventional display with highlighted regions enlarged showing the pre-edge region for the 1 s → 3d transitions, and the transition edge region for the 1 s → 4pz transitions

^{3}($3dx^2$-y^2, $3dz^2$) configuration, where $3dx^2$-y^2 and $3dz^2$ MOs are each singly occupied. The T_1 state returns to the ground state in approximately 200 ps.

By ps XANES (Fig. 1.17a), Chen et al. found a single peak appears in the pre-edge region due to the 1 s → $3dx^2$-y^2 transition in the S_0 state, while two peaks due to the 1 s → $3dx^2$-y^2 and 1 s → $3dz^2$ transitions are observed in the excited T_1 state, showing for the first time that indeed the latter has two singly occupied $3dx^2$-y^2 and $3dz^2$ MOs (Fig. 1.17b), which was only know from quantum chemical calculations. These results show the power of time-resolved XAS at unraveling the electronic structure of transient species that are optically silent. In addition, from the EXAFS they also obtained the geometry changes of the excited system, as well as following the ligation processes that occur with some solvents [173].

The next stage along this line of results is the study of metalloproteins and in particular, haemoproteins. As a matter of fact the first time-resolved XAS ever to be carried out were on ligated myoglobins, [121, 174–179] but were all limited to the microsecond time scale. This time resolution is sufficient for the CO ligand, and for other ligands if the system is at low temperature, which was the case in some of these studies. To get at the dynamics at room temperature, one would need to reach the ps, and possibly the fs tme resolution [180–183]. In order to reach the ps resolution and exploiting its enhanced sensitivity, the Lausanne group implemented the high repetition rate scheme described in Sect. 1.2 and [115]. A first result on the photodissociation of CO from carboxymyoglobin (MbCO) is shown in Fig. 1.18. Because of the long recombination time of CO to Mb (milliseconds), this results was not obtained with the pulse-to-pulse data acquisition

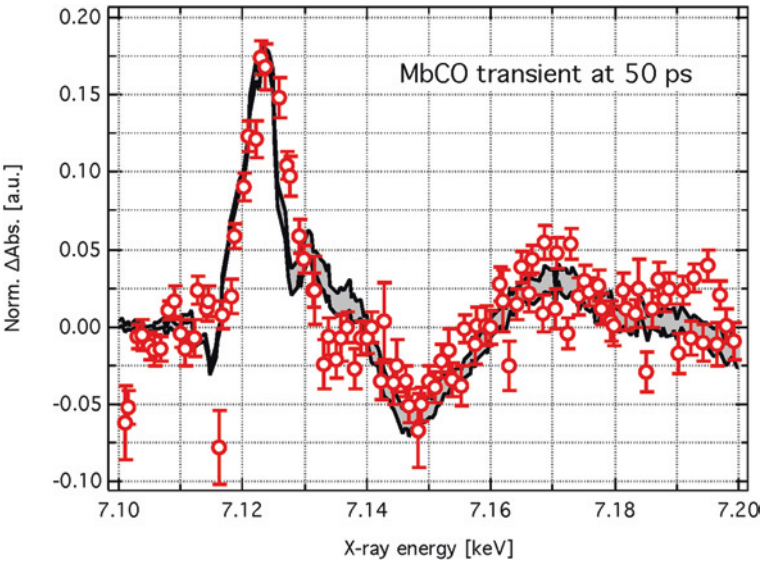

Fig. 1.18 Transient XAS of 2 mM MbCO collected in fluorescence mode. The sample was excited at 532 nm. The black curve represents the difference XAS based on the static spectra of deoxyMb and MbCO and scaled by 21 % (after [115])

described in Sect. 1.2. Rather the spectra were accumulated at tens of ps time delay with and without the laser on. Figure 1.18 shows that the transient spectrum is similar to the difference of the ligated minus unligated (deoxy form) spectra of Myoglobin, confirming that the data acquisition strategy is sound. This study was then extended to probing the recombination dynamics of MbNO, whose time scale is about 200 ps. This was done using the pulse-to-pulse data acquisition and the results fully confirm the recombination time derived from optical-only studies [184]. These first results confirm that ps XAS can be implemented on biological systems and open the way to the study of ligand dynamics with time resolution of better than 100 ps. They are also important forgoing studies for the preparation of experiments to be carried out at the X-ray free electron laser.

1.5 Conclusion and Outlook

The above review presented the recent advances in picosecond and femtosecond X-ray absorption spectroscopy but it is not exhaustive. The more recent activities of the Argonne group on molecular systems in liquids have been reviewed in [59]. This review also does not include the numerous ps and fs XAS studies carried out on solid materials, which have led to a wealth of new results in condensed matter physics on highly correlated systems, [42, 185–187] on semiconductors, [188] on phase

transitions, [100, 101, 189–192] defect formation in solids, [193] and on the spin dynamics in materials [194].

Ps XAS (and to a lesser extent fs XAS) can be considered as a routine technique that can be implemented to a large class of molecular systems in solution, but also to the probing of atomic ions in solutions, as recently demonstrated in the case of aqueous Iodide [166] and Bromide [167]. These studies presented above, have been limited to the systems containing heavy atoms, since the solvent absorption is weak in the hard X-ray range. Furthermore, they have been limited to chemical systems, even though the desire to carry out studies on biological systems in physiological media has been stressed in the introduction to the technique, and as already mentioned, the first time-resolved XAS was carried out on biological systems [121]. Such studies are still commonly being carried out with milli- to microsecond resolution [148, 149, 170, 178, 179, 195, 196]. One of the aims of current efforts is to extend them to higher temporal resolutions.

Several exciting prospects are on the way thanks to recent developments in the implementation of methodologies:

a. All the above experiments were carried out using a pump laser at 1 kHz repetition rate, while the storage ring operates at MHz repetition rates. This implies that typically 10^3 X-ray photons remain unused. The implementation of high repetition rate lasers (running at hundreds of kHz) that match an integer fraction of the storage ring repetition rate, combined with microfocussing of the X-ray and laser beams (this is possible at several synchrotron beam lines) allow a significant increase of signal to noise, and therefore, the possibility to reduce the data acquisition times and to work at much lower dilutions that in the present situation (tens of millimolar), thus approaching the concentration of biological samples [115]. In addition the compactness of the high repetition rate laser systems allow for a large flexibility in portability and simplification of the experimental set-up. Last but not least, the use of the high repetition rate laser allows for new experiments such as X-ray emission (XES), [197] resonant inelastic X-ray scattering (RIXS) and X-ray diffraction (XRD) and scattering (XRS). As a matter of fact, recent work by Bressler et al. [198] have indeed shown all these capabilities.
b. Now that femtosecond XAS been demonstrated [36, 38, 39] thanks to the slicing scheme, more studies should be possible. However the main limitation of the slicing scheme is its very low flux, and more hope is now put on the free electron lasers which deliver orders of magnitude more flux. Recently, femtosecond resolved XAS spectra at the Fe K edge were recorded at a commissioning beamtime at the LCLS Stanford, demonstrating very short data acquisition times [199].
c. Extension of time-resolved XAS to the soft X-ray regime [57, 58], and the recent results by Huse et al., both in the ps [119, 120] as well as the fs time domain [37], show the anticipated returns from such a technique. The recent static soft X-ray studies of biological systems in physiological solutions [200] also open the way to their study in the time domain. Furthermore, the recent

demonstration of a strong interaction of aqueous solvents with metal centres in various types of complexes, offers a new way of probing the role of the solvents in affecting the electronic structure of solutes, [201] but here again, when transferred to the time-domain these studies will deliver an additional degree of insight. These approaches have already yielded a wealth of new results on chemical systems.

d. Core-level spectroscopies, such as Auger spectroscopy, X-ray emission spectroscopy (XES), ultraviolet photoelectron spectroscopy (UPS) and X-ray photoelectron spectroscopy (XPS) are very well established techniques to probe the *electronic* structure of molecular systems, and have also been implemented in the static mode on high vapour pressure liquids [118]. Their extension into the time domain is also underway, and recent femtosecond UPS results were reported on various species in solution using a high harmonic VUV source, [202–205] while the first ps XES and RIXS studies on $[Fe^{II}(bpy)_3]$ have also been reported [197, 198].

In conclusion, the prospects are bright for ultrafast X-ray absorption spectroscopy studies. While the upcoming X-ray free electron lasers offer a dramatic increase in flux and time resolution, with very exciting prospects, accessability is limited since these are single user machines. Therefore, synchrotrons will remain the main source of X-ray photons for such applications, especially that they will allow preliminary and complementary studies to those carried out at XFELs.

Acknowledgments Deep thanks to all my co-workers who have contributed to the various studies presented here, and in particular to Ch. Bressler, C. Milne, W. Gawelda, V.-T. Pham, R. M. van der Veen, T. Penfold and F. van Mourik. We also acknowledge the great collaboration with the team at the MicroXAS beamline of the Swiss Light Source (PSI, Villigen): S. Johnson, P. Beaud, D. Grolimund, C. N. Borca, G. Ingold and R. Abela. Many thanks to M. Benfatto, P. D'Angelo (Rome), I. Tavernelli (Lausanne) and A. Hauser (Geneva) for useful discussions and samples.

References

1. A.H. Zewail, J. Phys. Chem. A **104**, 5660 (2000)
2. A.H. Zewail, Angew. Chem. Int. Edit. **39**, 2587 (2000)
3. R. Henderson, Q. Rev. Biophys. **28**, 171 (1995)
4. R. Srinivasan, V.A. Lobastov, C.Y. Ruan, A.H. Zewail, Helv. Chim. Acta **86**, 1763 (2003)
5. A.H. Zewail, Annu. Rev. Phys. Chem. **57**, 65 (2006)
6. V.A. Lobastov, R. Srinivasan, A.H. Zewail, P. Natl. Acad. Sci. USA **102**, 7069 (2005)
7. S. Chen, M.T. Seidel, A.H. Zewail, Angew. Chem. Int. Edit. **45**, 5154 (2006)
8. V.A. Lobastov, J. Weissenrieder, J. Tang, A.H. Zewail, Nano Lett. **7**, 2552 (2007)
9. D. Shorokhov, A.H. Zewail, Phys. Chem. Chem.Phys. **10**, 2879 (2008)
10. M. Chergui, A.H. Zewail, Chem. Phys. Chem **10**, 28 (2009)
11. A.H. Zewail, J.M. Thomas, *4D electron microscopy : imaging in space and time* (Imperial College Press; Distributed by World Scientific Pub, London Hackensack, 2010)
12. F. Carbone, B. Barwick, O.H. Kwon, H.S. Park, J.S. Baskin, A.H. Zewail, Chem. Phys. Lett. **468**, 107 (2009)
13. F. Carbone, O.H. Kwon, A.H. Zewail, Science **325**, 181 (2009)

14. B. Barwick, D.J. Flannigan, A.H. Zewail, Nature **462**, 902 (2009)
15. F. Carbone, P. Musumeci, O.J. Luiten, C. Hebert, Chem. Phys. **392**, 1 (2012)
16. J.M. Thomas, P.A. Midgley, Chem. Phys. **385**, 1 (2011)
17. L. Guerin, E. Collet, M.B.L. Cointe, M.H. Lemee-Cailleau, H. Cailleau, M. Wulff, S. Techert, S.Y. Koshihara, J. Phys. IV **114**, 99 (2004)
18. L. Guerin, E. Collet, M.H. Lemee-Cailleau, Buron-Le Cointe, M.; Cailleau, H.; Plech, A.; Wulff, M.; Koshihara, S. Y.; Luty, T. Chem. Phys. **299**, 163 (2004)
19. F. Schotte, M.H. Lim, T.A. Jackson, A.V. Smirnov, J. Soman, J.S. Olson, G.N. Phillips, M. Wulff, P.A. Anfinrud, Science **2003**, 300 (1944)
20. E. Collet, M.H. Lemee-Cailleau, Buron-Le Cointe, M.; Cailleau, H.; Wulff, M.; Luty, T.; Koshihara, S. Y.; Meyer, M.; Toupet, L.; Rabiller, P.; Techert, S. Science **300**, 612 (2003)
21. F. Schotte, P.A. Anfinrud, G. Hummer, M. Wulff, Biophys. J. **86**, 525A (2004)
22. H. Ihee, M. Lorenc, T.K. Kim, Q.Y. Kong, M. Cammarata, J.H. Lee, S. Bratos, M. Wulff, Science **309**, 1223 (2005)
23. L. Guerin, J. Hebert, M.B.L. Cointe, S. Adachi, S. Koshihara, H. Cailleau, E. Collet, Phys Rev Lett. **105** (2010)
24. S. Bratos, F. Mirloup, R. Vuilleumier, M. Wulff, J. Chem. Phys. **116**, 10615 (2002)
25. J. Davidsson, J. Poulsen, M. Cammarata, P. Georgiou, R. Wouts, G. Katona, F. Jacobson, A. Plech, M. Wulff, G. Nyman, R. Neutze, Phys. Rev. Lett. **94**, 125509 (2005)
26. M. Cammarata, M. Lorenc, T.K. Kim, J.H. Lee, Q.Y. Kong, E. Pontecorvo, Lo Russo, M.; Schiro, G.; Cupane, A.; Wulff, M.; Ihee, H. J. Chem. Phys. **124**, 124504 (2006)
27. M. Christensen, K. Haldrup, K. Bechgaard, R. Feidenhans'l, Q.Y. Kong, M. Cammarata, Lo Russo, M.; Wulff, M.; Harrit, N.; Nielsen, M. M. J. Am. Chem. Soc. **131**, 502 (2009)
28. K. Haldrup, M. Christensen, M. Cammarata, Q.Y. Kong, M. Wulff, S.O. Mariager, K. Bechgaard, R. Feidenhans'l, N. Harrit, M.M. Nielsen, Angew. Chem. Int. Edit. **48**, 4180 (2009)
29. T.K. Kim, J.H. Lee, M. Wulff, Q.Y. Kong, H. Ihee, Chem. Phys. Chem. **2009**, 10 (1958)
30. S.L. Johnson, C.J. Milne, Trac-Trend Anal. Chem. **29**, 497 (2010)
31. R.W. Schoenlein, S. Chattopadhyay, H.H.W. Chong, T.E. Glover, P.A. Heimann, C.V. Shank, A.A. Zholents, M.S. Zolotorev, Science **287**, 2237 (2000)
32. R.W. Schoenlein, H.H.W. Chong, T.E. Glover, P.A. Heimann, W.P. Leemans, H.A. Padmore, C.V. Shank, A.A. Zholents, M.S. Zolotorev, J.S. Corlett, Cr. Acad. Sci. IV-Phys. **2**, 1373 (2001)
33. S. Khan, K. Holldack, T. Kachel, R. Mitzner, T. Quast, Phys. Rev. Lett. **97**, 074801 (2006)
34. P. Beaud, S.L. Johnson, A. Streun, R. Abela, D. Abramsohn, D. Grolimund, F. Krasniqi, T. Schmidt, V. Schlott, G. Ingold, Phys. Rev. Lett. **99**, 174801 (2007)
35. S.L. Johnson, P. Beaud, E. Vorobeva, C.J. Milne, E.D. Murray, S. Fahy, G. Ingold, Acta Crystallogr. A **66**, 157 (2010)
36. C. Bressler, C. Milne, V.T. Pham, A. ElNahhas, R.M. van der Veen, W. Gawelda, S. Johnson, P. Beaud, D. Grolimund, M. Kaiser, C.N. Borca, G. Ingold, R. Abela, M. Chergui, Science **323**, 489 (2009)
37. H.D. Wen, N. Huse, R.W. Schoenlein, A.M. Lindenberg, J Chem Phys **131**, 234505 (2009)
38. N. Huse, H. Cho, K. Hong, L. Jamula, F.M.F. de Groot, T.K. Kim, J.K. McCusker, R. Schoenlein, J. Phys. Chem. Lett. **2**, 880 (2011)
39. V.T. Pham, T.J. Penfold, R.M. van der Veen, F. Lima, A. El Nahhas, S.L. Johnson, P. Beaud, R. Abela, C. Bressler, I. Tavernelli, C.J. Milne, M. Chergui, J. Am. Chem. Soc. **133**, 12740 (2011)
40. C. Rose-Petruck, R. Jimenez, T. Guo, A. Cavalleri, C.W. Siders, F. Raksi, J.A. Squier, B.C. Walker, K.R. Wilson, C.P.J. Barty, Nature **398**, 310 (1999)
41. C.W. Siders, A. Cavalleri, K. Sokolowski-Tinten, C. Toth, T. Guo, M. Kammler, M.H. von Hoegen, K.R. Wilson, D. von der Linde, C.P.J. Barty, Science **286**, 1340 (1999)
42. A. Cavalleri, R.W. Schoenlein, Ultrafast Dyn. Processes Semiconductors **92**, 309 (2004)
43. M. Bargheer, N. Zhavoronkov, M. Woerner, T. Elsaesser, Chem. Phys. Chem. **7**, 783 (2006)
44. K.J. Gaffney, H.N. Chapman, Science **316**, 1444 (2007)
45. C.V. Schmising, M. Bargheer, M. Woerner, T. Elsaesser, Zeitschrift Fur Kristallographie **223**, 283 (2008)

46. G. Ingold, R. Abela, P. Beaud, S.L. Johnson, U. Staub, Zeitschrift Fur Kristallographie **223**, 292 (2008)
47. S.L. Johnson, P. Beaud, C.J. Milne, F.S. Krasniqi, E.S. Zijlstra, M.E. Garcia, M. Kaiser, D. Grolimund, R. Abela, G. Ingold, Phys. Rev. Lett. **100**, 155501 (2008)
48. C.V.K. Schmising, M. Bargheer, M. Kiel, N. Zhavoronkov, M. Woerner, T. Elsaesser, I. Vrejoiu, D. Hesse, M. Alexe, Phys. Rev. Lett. **98**, 248301 (2007)
49. M. Woerner, F. Zamponi, Z. Ansari, J. Dreyer, B. Freyer, M. Premont-Schwarz, T. Elsaesser, J. Chem. Phys. **133**, 064509 (2010)
50. F. Zamponi, Z. Ansari, M. Woerner, T. Elsaesser, Opt. Express **18**, 947 (2010)
51. M. BenNun, J.S. Cao, K.R. Wilson, J. Phys. Chem. A **101**, 8743 (1997)
52. J.S. Cao, K.R. Wilson, J. Phys. Chem. A **102**, 9523 (1998)
53. J.P. Bergsma, M.H. Coladonato, P.M. Edelsten, J.D. Kahn, K.R. Wilson, D.R. Fredkin, J. Chem. Phys. **84**, 6151 (1986)
54. H. Ihee, Accounts. Chem. Res. **42**, 356 (2009)
55. L.X. Chen, J. Electron Spectrosc. **119**, 161 (2001)
56. L.X. Chen, Angew. Chem. Int. Edit. **43**, 2886 (2004)
57. C. Bressler, M. Chergui, Chem. Rev. **104**, 1781 (2004)
58. C. Bressler, R. Abela, M. Chergui, Zeitschrift Fur Kristallographie **223**, 307 (2008)
59. L.X. Chen, X.Y. Zhang, J.V. Lockard, A.B. Stickrath, K. Attenkofer, G. Jennings, D.J. Liu, Acta Crystallogr. A **66**, 240 (2010)
60. C. Bressler, M. Chergui, Annu. Rev. Phys. Chem. **61**, 263 (2010)
61. M. Chergui, Acta Crystallogr. A **66**, 229 (2010)
62. D.C. Koningsberger, R. Prins, *X-ray absorption : principles, applications, techniques of EXAFS, SEXAFS, and XANES* (Wiley, New York, 1988)
63. J. Stöhr, *NEXAFS spectroscopy* (Springer, Berlin etc., 1992)
64. J.J. Rehr, R.C. Albers, Rev. Mod. Phys. **72**, 621 (2000)
65. E.A. Stern, Phys. Rev. B **10**, 3027 (1974)
66. D.E. Sayers, E.A. Stern, F.W. Lytle, Phys. Rev. Lett. **27**, 1204 (1971)
67. A. Filipponi, J. Phys.-Condens. Mat. **6**, 8415 (1994)
68. A.L. Ankudinov, C.E. Bouldin, J.J. Rehr, J. Sims, H. Hung, Phys. Rev. B **65**, 104 (2002)
69. J.J. Rehr, J.J. Kas, F.D. Vila, M.P. Prange, K. Jorissen, Phys. Chem. Chem. Phys. **12**, 5503 (2010)
70. A.L. Ankudinov, B. Ravel, J.J. Rehr, S.D. Conradson, Phys. Rev. B **58**, 7565 (1998)
71. C.R. Natoli, M. Benfatto, Della Longa, S.; Hatada, K. J. Synchrotron Radiat. **10**, 26 (2003)
72. J.J. Rehr, J.J. Kas, M.P. Prange, A.P. Sorini, Y. Takimoto, F. Vila, C.R. Phys. **10**, 548 (2009)
73. B. Ravel, M. Newville, J. Synchrotron Radiat. **12**, 537 (2005)
74. J.L. Beeby, Proc. R Soc. Lon. Ser.-A **279**, 82 (1964)
75. C.A. Ashley, S. Doniach, Phys. Rev. B **11**, 1279 (1975)
76. P. Lloyd, P.V. Smith, Adv. Phys. **21**, 69 (1972)
77. T.A. Tyson, M. Benfatto, C.R. Natoli, B. Hedman, K.O. Hodgson, Phys. B **158**, 425 (1989)
78. T.A. Tyson, K.O. Hodgson, C.R. Natoli, M. Benfatto, Phys. Rev. B **46**, 5997 (1992)
79. C.R. Natoli, M. Benfatto, S. Doniach, Phys. Rev. A **34**, 4682 (1986)
80. M. Benfatto, Della Longa, S.; Hatada, K.; Hayakawa, K.; Gawelda, W.; Bressler, C.; Chergui, M. J. Phys. Chem. B **110**, 14035 (2006)
81. S.I. Zabinsky, J.J. Rehr, A. Ankudinov, R.C. Albers, M.J. Eller, Phys. Rev. B **52**, 2995 (1995)
82. J. Mustre, Y. Yacoby, E.A. Stern, J.J. Rehr, Phys. Rev. B **42**, 10843 (1990)
83. W. Gawelda, V.T. Pham, R.M. van der Veen, D. Grolimund, R. Abela, M. Chergui, C. Bressler, J. Chem. Phys. **130**, 124520 (2009)
84. K. Okada, A. Kotani, B.T. Thole, J. Electron Spectrosc. **58**, 325 (1992)
85. B.T. Thole, G. Vanderlaan, J.C. Fuggle, G.A. Sawatzky, R.C. Karnatak, J.M. Esteva, Phys. Rev. B **32**, 5107 (1985)
86. F. De Groot, Coordin. Chem. Rev. **249**, 31 (2005)

87. F. De Groot, A. Kotani, *Core Level Spectroscopy of Solids* (Taylor & Francis, New York, 2008)
88. W. Gawelda, M. Johnson, F.M.F. de Groot, R. Abela, C. Bressler, M. Chergui, J. Am. Chem. Soc. **128**, 5001 (2006)
89. F. De Groot, Chem. Rev. **101**, 1779 (2001)
90. A. Bianconi, In X-ray absorption principles, applications, techniques of exafs, sexafs and xanes, ed. by D. C. Koningsberger, R. Prins, (Wiley, New York, 1988), p 12
91. M. Benfatto, Della Longa, S.; Natoli, C. R. J. Synchrotron Radiat. **10**, 51 (2003)
92. M. Benfatto, D.S. Longa, J. Synchrotron Radiat. **1087**, 8 (2001)
93. W. Gawelda, V.T. Pham, A. El Nahhas, M. Kaiser, Y. Zaushytsin, S. Johnson, D. Grolimund, R. Abela, A. Hauser, C. Bressler, M. Chergui, AIP Conf. Proc. **882**, 31 (2007)
94. A.A. Zholents, M.S. Zolotorev, Phys. Rev. Lett. **76**, 912 (1996)
95. K. Murakami, H.C. Gerritsen, H. Vanbrug, F. Bijkerk, F.W. Saris, M.J. Vanderwiel, Phys. Rev. Lett. **56**, 655 (1986)
96. K. O. T. Murakami, A. Miyashita, O. Yoda, AIP Conference Proceedings, Vol. 228, p. 375 (1994)
97. F. Raksi, K.R. Wilson, Z.M. Jiang, A. Ikhlef, C.Y. Cote, J.C. Kieffer, J. Chem. Phys. **104**, 6066 (1996)
98. I.V. Tomov, D.A. Oulianov, P.L. Chen, P.M. Rentzepis, J. Phys. Chem. B **103**, 7081 (1999)
99. F. Benesch, T.W. Lee, Y. Jiang, C.G. Rose-Petruck, Opt. Lett. **2004**, 29 (1028)
100. K. Oguri, Y. Okano, T. Nishikawa, H. Nakano, Appl. Phys. Lett. **87**, 011503 (2005)
101. Y. Okano, K. Oguri, T. Nishikawa, H. Nakano, Rev. Sci. Instrum. **77**, 046105 (2006)
102. K. Hatanaka, T. Miura, H. Fukumura, Appl. Phys. Lett. **80**, 3925 (2002)
103. T. Lee, Y. Jiang, C.G. Rose-Petruck, F. Benesch, J. Chem. Phys. **122**, 84506 (2005)
104. T. Guo, Laser Photonics Rev. **3**, 591 (2009)
105. T. Elsaesser, M. Woerner, Acta Crystallogr. A **66**, 168 (2010)
106. C. Bressler, M. Saes, M. Chergui, D. Grolimund, R. Abela, P. Pattison, J. Chem. Phys. **116**, 2955 (2002)
107. C. Bressler, M. Saes, M. Chergui, R. Abela, P. Pattison, Nucl. Instrum. Meth. A **467**, 1444 (2001)
108. M. Saes, W. Gawelda, M. Kaiser, A. Tarnovsky, C. Bressler, M. Chergui, S.L. Johnson, D. Grolimund, R. Abela, Synchrotron Radiat. News **16**, 12 (2003)
109. M. Saes, C. Bressler, F. van Mourik, W. Gawelda, M. Kaiser, M. Chergui, C. Bressler, D. Grolimund, R. Abela, T.E. Glover, P.A. Heimann, R.W. Schoenlein, S.L. Johnson, A.M. Lindenberg, R.W. Falcone, Rev. Sci. Instrum. **75**, 24 (2004)
110. W. Gawelda, C. Bressler, M. Saes, M. Kaiser, A. Tarnovsky, D. Grolimund, S.L. Johnson, R. Abela, M. Chergui, Phys. Scr. **T115**, 102 (2005)
111. T. Giessel, D. Brocker, P. Schmidt, W. Widdra, Rev. Sci. Instrum. **74**, 4620 (2003)
112. W. Widdra, D. Brocker, T. Giessel, I.V. Hertel, W. Kruger, A. Liero, F. Noack, V. Petrov, D. Pop, P.M. Schmidt, R. Weber, I. Will, B. Winter, Surf. Sci. **543**, 87 (2003)
113. P. Fons, D. Brewe, E. Stern, A.V. Kolobov, J. Tominaga, Mater Res. Soc. Symp. P **918**, 147 (2006)
114. E.A. Stern, D. Brewe, AIP Conf. Proc. **882**, 24 (2007)
115. F.A. Lima, C.J. Milne, D.C.V. Amarasinghe, M.H. Rittmann-Frank, R.M. van der Veen, M. Reinhard, V.T. Pham, S. Karlsson, S.L. Johnson, D. Grolimund, C. Borca, T. Huthwelker, M. Janousch, F. van Mourik, R. Abela, M. Chergui, Rev. Sci. Instrum. **82**, 063111 (2011)
116. F.M.F. De Groot, J. Vogel, (Oxford University Press, Oxford, 2004)
117. A. Nilsson, L.G.M. Pettersson, Chem. Phys. **389**, 1 (2011)
118. B. Winter, M. Faubel, Chem. Rev. **106**, 1176 (2006)
119. G. Gavrila, K. Godehusen, C. Weniger, E.T.J. Nibbering, T. Elsaesser, W. Eberhardt, P. Wernet, Appl. Phys. A-Mater. **96**, 11 (2009)
120. N. Huse, Private communication
121. D.M. Mills, A. Lewis, A. Harootunian, J. Huang, B. Smith, Science **223**, 811 (1984)

122. H.B. Gray, J.R. Winkler, Annu. Rev. Biochem. **65**, 537 (1996)
123. H. B. Gray, *In Electron transfer in chemistry,* ed. by V. Balzani, (Wiley-VCH, Weinheim, 2001)
124. A. Juris, V. Balzani, F. Barigelletti, S. Campagna, P. Belser, A. Vonzelewsky, Coordin. Chem. Rev. **84**, 85 (1988)
125. M. Gratzel, Nature **414**, 338 (2001)
126. M. Saes, C. Bressler, R. Abela, D. Grolimund, S.L. Johnson, P.A. Heimann, M. Chergui, Phys. Rev. Lett. **90**, 047403 (2003)
127. A.N. Tarnovsky, W. Gawelda, M. Johnson, C. Bressler, M. Chergui, J. Phys. Chem. B **110**, 26497 (2006)
128. F.M.F. De Groot, Z.W. Hu, M.F. Lopez, G. Kaindl, F. Guillot, M. Tronc, J. Chem. Phys. **101**, 6570 (1994)
129. G. Calzaferri, R. Rytz, J. Phys. Chem.-Us **99**, 12141 (1995)
130. E. König, K.J. Watson, Chem. Phys. Lett. **6**, 457 (1970)
131. K. Nozaki, K. Takamori, Y. Nakatsugawa, T. Ohno, Inorg. Chem. **45**, 6161 (2006)
132. F. Alary, J.L. Heully, L. Bijeire, P. Vicendo, Inorg. Chem. **46**, 3154 (2007)
133. G.B. Shaw, C.D. Grant, H. Shirota, E.W. Castner, G.J. Meyer, L.X. Chen, J. Am. Chem. Soc. **129**, 2147 (2007)
134. M. Iwamura, S. Takeuchi, T. Tahara, J. Am. Chem. Soc. **129**, 5248 (2007)
135. M. Iwamura, H. Watanabe, K. Ishii, S. Takeuchi, T. Tahara, Springer Ser. Chem. **92**, 382 (2009)
136. L.X. Chen, G.B. Shaw, I. Novozhilova, T. Liu, G. Jennings, K. Attenkofer, G.J. Meyer, P. Coppens, J. Am. Chem. Soc. **125**, 7022 (2003)
137. G. Smolentsev, A.V. Soldatov, L.X. Chen, J. Phys. Chem. A **112**, 5363 (2008)
138. T.J. Penfold, S. Karlsson, G. Capano, F.A. Lima, J. Rittmann, M.H. Rittmann-Frank, M. Reinhard, O. Bräm, E. Baranoff, R. Abela, I. Tavernelli, U. Röthlisberger, C. Milne, M. Chergui, J. Phys. Chem. A 117, 4591–4601 (2013)
139. T. J. Penfold, B.F.E. Curchod, I. Tavernelli, R. Abela, U. Röthlisberger, M. Chergui, Phys. Chem. Chem. Phys. 14, 9444–9450 (2012)
140. A. Vlcek, Coordin. Chem. Rev. **200**, 933 (2000)
141. R.M. van der Veen, C.J. Milne, A. El Nahhas, F.A. Lima, V.T. Pham, J. Best, J.A. Weinstein, C.N. Borca, R. Abela, C. Bressler, M. Chergui, Angew. Chem. Int. Edit. **48**, 2711 (2009)
142. I.V. Novozhilova, A.V. Volkov, P. Coppens, J. Am. Chem. Soc. **2003**, 125 (1079)
143. J.V. Lockard, A.A. Rachford, G. Smolentsev, A.B. Stickrath, X.H. Wang, X.Y. Zhang, K. Atenkoffer, G. Jennings, A. Soldatov, A.L. Rheingold, F.N. Castellano, L.X. Chen, J. Phys. Chem. A **114**, 12780 (2010)
144. R.M. van der Veen, C. Bressler, C.J. Milne, V.T. Pham, A. El Nahhas, F.A. Lima, W. Gawelda, C.N. Borca, R. Abela, M. Chergui, J. Phys. Conf. Ser. **190**, 012052 (2009)
145. A. Hauser, *Spin Crossover in Transition Metal Compounds II.*(Springer, Berlin, 2004), Vol. 234, p. 155
146. B. Ordejon, C. de Graaf, C. Sousa, J. Am. Chem. Soc. **130**, 13961 (2008)
147. P. Guionneau, M. Marchivie, G. Bravic, J.F. Letard, D. Chasseau, Top. Curr. Chem. **234**, 97 (2004)
148. H. Oyanagi, T. Tayagaki, K. Tanaka, J. Phys. Chem. Solids **65**, 1485 (2004)
149. H. Oyanagi, T. Tayagaki, K. Tanaka, J. Lumin. **119**, 361 (2006)
150. L.M.L. Daku, A. Vargas, A. Hauser, A. Fouqueau, M.E. Casida, Chem. Phys. Chem. **6**, 1393 (2005)
151. M. Khalil, M.A. Marcus, A.L. Smeigh, J.K. McCusker, H.H.W. Chong, R.W. Schoenlein, J. Phys. Chem. A **110**, 38 (2006)
152. W. Gawelda, V.T. Pham, M. Benfatto, Y. Zaushytsin, M. Kaiser, D. Grolimund, S. Johnson, R. Abela, C. Bressler, M. Chergui, Phys. Rev. Lett. **98**, 057401 (2007)
153. J.E. Monat, J.K. McCusker, J. Am. Chem. Soc. **122**, 4092 (2000)
154. E.A. Juban, A.L. Smeigh, J.E. Monat, J.K. McCusker, Coordin. Chem. Rev. **250**, 1783 (2006)
155. J.K. McCusker, A.L. Rheingold, D.N. Hendrickson, Inorg. Chem. **35**, 2100 (1996)
156. W. Gawelda, A. Cannizzo, V.T. Pham, F. van Mourik, C. Bressler, M. Chergui, J. Am. Chem. Soc. **129**, 8199 (2007)

157. V. Briois, P. Sainctavit, G.J. Long, F. Grandjean, Inorg. Chem. **40**, 912 (2001)
158. J.P. Tuchagues, A. Bousseksou, G. Molnar, J.J. McGarvey, F. Varret, Top. Curr. Chem. **235**, 85 (2004)
159. A. Cannizzo, C.J. Milne, C. Consani, W. Gawelda, C. Bressler, F. van Mourik, M. Chergui, Coordin. Chem. Rev. **254**, 2677 (2010)
160. O. Bram, A. Cannizzo, A.A. Oskouei, A. Tortschanoff, F. van Mourik, M. Chergui, Springer Ser. Chem. **92**, 346 (2009)
161. N. Huse, H.D. Wen, D. Nordlund, E. Szilagyi, D. Daranciang, T.A. Miller, A. Nilsson, R.W. Schoenlein, A.M. Lindenberg, Phys. Chem. Chem. Phys. **11**, 3951 (2009)
162. P. Wernet, G. Gavrila, K. Godehusen, C. Weniger, E.T.J. Nibbering, T. Elsaesser, W. Eberhardt, Appl. Phys. A-Mater **92**, 511 (2008)
163. M. Maroncelli, J. Mol. Liq. **57**, 1 (1993)
164. R.M. Stratt, M. Maroncelli, J. Phys. Chem.-Us **100**, 12981 (1996)
165. S.K. Pal, A.H. Zewail, Chem. Rev. **104**, 2099 (2004)
166. V.T. Pham, W. Gawelda, Y. Zaushytsin, M. Kaiser, D. Grolimund, S. Johnson, R. Abela, C. Bressler, M. Chergui, J. Am. Chem. Soc. **129**, 1530 (2007)
167. C.G. Elles, I.A. Shkrob, R.A. Crowell, D.A. Arms, E.C. Landahl, J. Chem. Phys. **128**, 061102 (2008)
168. V.T. Pham, I. Tavernelli, C.J. Milne, R.M. van der Veen, P. D'Angelo, C. Bressler, M. Chergui, Chem. Phys. **371**, 24 (2010)
169. K.M. Kadish, K.M. Smith, R. Guilard, *The porphyrin handbook* (Academic Press, San Diego, 2000)
170. L.X. Chen, P.L. Lee, D. Gosztola, W.A. Svec, P.A. Montano, M.R. Wasielewski, J. Phys. Chem. B **103**, 3270 (1999)
171. L.X. Chen, W.J.H. Jager, G. Jennings, D.J. Gosztola, A. Munkholm, J.P. Hessler, Science **292**, 262 (2001)
172. L.X. Chen, X.Y. Zhang, E.C. Wasinger, K. Attenkofer, G. Jennings, A.Z. Muresan, J.S. Lindsey, J. Am. Chem. Soc. **129**, 9616 (2007)
173. S. Della-Longa, L.X. Chen, P. Frank, K. Hayakawa, K. Hatada, M. Benfatto, Inorg. Chem. **48**, 3934 (2009)
174. D.M. Mills, Acta Crystallogr. A **40**, C393 (1984)
175. A. Clozza, A.C. Castellano, S. Dellalonga, A. Giovannelli, A. Bianconi, Rev. Sci. Instrum. **60**, 2519 (1989)
176. M.R. Chance, M.D. Wirt, E.M. Scheuring, L.M. Miller, A.H. Xie, D.E. Sidelinger, Rev. Sci. Instrum. **64**, 2035 (1993)
177. L. Powers, B. Chance, M. Chance, B. Campbell, J. Friedman, S. Khalid, C. Kumar, A. Naqui, K.S. Reddy, Y. Zhou, Biochem.-Us **26**, 4785 (1987)
178. A. Arcovito, D.C. Lamb, G.U. Nienhaus, J.L. Hazemann, M. Benfatto, S.D. Longa, Biophys. J. **88**, 2954 (2005)
179. H.X. Wang, G. Peng, S.P. Cramer, J. Electron Spectrosc. **143**, 1 (2005)
180. J.L. Martin, M.H. Vos, Annu. Rev. Biophys. Biomol. Struct. **21**, 199 (1992)
181. M. Vos, Actual Chimique, **52** (2008)
182. M.H. Vos, Bba-Bioenerg. **1777**, 15 (2008)
183. M. Chergui, *Advances in Accounting Behavioral Research (BIPH)* (Elsevier: Amsterdam, 2011) (Vol. Comprehensive Biophysics)
184. F. A. Lima, E. A. In preparation (2012)
185. A. Cavalleri, H.H.W. Chong, S. Fourmaux, T.E. Glover, P.A. Heimann, J.C. Kieffer, B.S. Mun, H.A. Padmore, R.W. Schoenlein, Phys. Rev. B **69**, 153106 (2004)
186. A. Cavalleri, M. Rini, H.H.W. Chong, S. Fourmaux, T.E. Glover, P.A. Heimann, J.C. Kieffer, R.W. Schoenlein, Phys. Rev. Lett. **95**, 067405 (2005)
187. A. Cavalleri, S. Wall, C. Simpson, E. Statz, D.W. Ward, K.A. Nelson, M. Rini, R.W. Schoenlein, Nature **442**, 664 (2006)
188. B.W. Adams, M.F. DeCamp, E.M. Dufresne, D.A. Reis, Rev. Sci. Instrum. **73**, 4150 (2002)

189. S.L. Johnson, P.A. Heimann, A.M. Lindenberg, H.O. Jeschke, M.E. Garcia, Z. Chang, R.W. Lee, J.J. Rehr, R.W. Falcone, Phys. Rev. Lett. **91**, 157403 (2003)
190. S.L. Johnson, P.A. Heimann, A.G. MacPhee, A.M. Lindenberg, O.R. Monteiro, Z. Chang, R.W. Lee, R.W. Falcone, Phys. Rev. Lett. **94**, 057407 (2005)
191. K. Oguri, H. Nakano, T. Nishikawa, N. Uesugi, Appl. Phys. Lett. **79**, 4506 (2001)
192. Y. Okano, K. Oguri, T. Nishikawa, H. Nakano, J. Appl. Phys. **99**, 063302 (2006)
193. E. Vorobeva, S.L. Johnson, P. Beaud, C.J. Milne, M. Benfatto, G. Ingold, Phys. Rev. B **80**, 134301 (2009)
194. C. Stamm, T. Kachel, N. Pontius, R. Mitzner, T. Quast, K. Holldack, S. Khan, C. Lupulescu, E.F. Aziz, M. Wietstruk, H.A. Durr, W. Eberhardt, Nat. Mater. **6**, 740 (2007)
195. M. Haumann, P. Liebisch, C. Muller, M. Barra, M. Grabolle, H. Dau, Science **2005**, 310 (1019)
196. M. Haumann, C. Muller, P. Liebisch, T. Neisius, H. Dau, J. Synchrotron Radiat. **12**, 35 (2005)
197. G. Vanko, P. Glatzel, V.T. Pham, R. Abela, D. Grolimund, C.N. Borca, S.L. Johnson, C.J. Milne, C. Bressler, Angew. Chem. Int. Edit. **49**, 5910 (2010)
198. C. Bressler, Private communication
199. C. Bressler, R. Abela, M. Cammarata, Private communication
200. E.F. Aziz, N. Ottosson, S. Bonhommeau, N. Bergmann, W. Eberhardt, M. Chergui, Phys. Rev. Lett. **102**, 68103 (2009)
201. E.F. Aziz, M.H. Rittmann-Frank, K.M. Lange, S. Bonhommeau, M. Chergui, Nat. Chem. **2**, 853 (2010)
202. O. Link, E. Lugovoy, K. Siefermann, Y. Liu, M. Faubel, B. Abel, Appl. Phys. A-Mater. **96**, 117 (2009)
203. A. Lubcke, F. Buchner, N. Heine, I.V. Hertel, T. Schultz, Phys. Chem. Chem. Phys. **12**, 14629 (2010)
204. Y. Tang, H. Shen, K. Sekiguchi, N. Kurahashi, T. Mizuno, Y.I. Suzuki, T. Suzuki, Phys. Chem. Chem. Phys. **12**, 3653 (2010)
205. Y. Tang, Y.I. Suzuki, H. Shen, K. Sekiguchi, N. Kurahashi, K. Nishizawa, P. Zuo, T. Suzuki, Chem. Phys. Lett. **494**, 111 (2010)
206. R.M. van der Veen, C.J. Milne, V.T. Pham, A. El Nahhas, J.A. Weinstein, J. Best, C.N. Borca, C. Bressler, M. Chergui, Chimia **62**, 287 (2008)
207. R.M. van der Veen, J.J. Kas, C.J. Milne, V.T. Pham, A. El Nahhas, F.A. Lima, D.A. Vithanage, J.J. Rehr, R. Abela, M. Chergui, Phys. Chem. Chem. Phys. **12**, 5551 (2010)
208. S.J. Lind, K.C. Gordon, M.R. Waterland, J. Raman Spectrosc. **39**, 1556 (2008)
209. L.X. Chen, G. Jennings, T. Liu, D.J. Gosztola, J.P. Hessler, D.V. Scaltrito, G.J. Meyer, J. Am. Chem. Soc. **124**, 10861 (2002)

http://www.springer.com/978-3-642-45151-5

In-situ Materials Characterization
Across Spatial and Temporal Scales
Ziegler, A.; Graafsma, H.; Zhang, X.F.; Frenken, J.W.M.
(Eds.)
2014, XI, 256 p. 124 illus., 78 illus. in color., Hardcover
ISBN: 978-3-642-45151-5